
# NAVAL POSTGRADUATE SCHOOL

**MONTEREY, CALIFORNIA**

# THESIS

**COLD SPRAYED COATINGS WITH DUAL NANOPARTICLE REINFORCEMENTS FOR WEAR AND CORROSION PROTECTION**

by

Travis Norrell

June 2020

| | |
|---|---|
| Thesis Advisor: | Andy Nieto |
| Second Reader: | Troy Ansell |

THIS PAGE INTENTIONALLY LEFT BLANK

| REPORT DOCUMENTATION PAGE | | | *Form Approved OMB No. 0704-0188* |
|---|---|---|---|



| **1. AGENCY USE ONLY** *(Leave blank)* | **2. REPORT DATE** June 2020 | **3. REPORT TYPE AND DATES COVERED** Master's thesis |
|---|---|---|

**4. TITLE AND SUBTITLE**
COLD SPRAYED COATINGS WITH DUAL NANOPARTICLE REINFORCEMENTS FOR WEAR AND CORROSION PROTECTION

**5. FUNDING NUMBERS**

**6. AUTHOR(S)** Travis Norrell

**7. PERFORMING ORGANIZATION NAME(S) AND ADDRESS(ES)**
Naval Postgraduate School
Monterey, CA 93943-5000

**8. PERFORMING ORGANIZATION REPORT NUMBER**

**9. SPONSORING / MONITORING AGENCY NAME(S) AND ADDRESS(ES)**
N/A

**10. SPONSORING / MONITORING AGENCY REPORT NUMBER**

**11. SUPPLEMENTARY NOTES** The views expressed in this thesis are those of the author and do not reflect the official policy or position of the Department of Defense or the U.S. Government.

**12a. DISTRIBUTION / AVAILABILITY STATEMENT**
Approved for public release. Distribution is unlimited.

**12b. DISTRIBUTION CODE**
A

**13. ABSTRACT (maximum 200 words)**

As a form of additive manufacturing, the use of cold spray has made significant strides since different-sized particles were explored in the process. There is proof that micron-sized particles down to nanoparticles enhance the mechanical material properties of a substrate in wear resistance. Micron- and submicron-sized particles are beneficial, but due to their low relative surface areas, they tend to exhibit pull out more often and do not adhere to a substrate as well as a nanoparticle. Using nanoparticle metal and dual ceramic matrix reinforcements, six composites were fabricated through cryomilling and then applied to an aluminum substrate as a cold sprayed coating. Using nano-boron carbide ($nB_4C$) and boron nitride nanoplatelets (BNNP) at various combinations up to 2 vol%, an increase of 11.59% in hardness from the control was achieved. Wear testing of each coating was performed, but most of the tests drove through the coatings into the substrate, indicating more refinement of the testing parameters is required. Additionally, corrosion testing was performed on cold sprayed samples for 500- and 2,000-hr trials in a salt fog chamber, revealing underlying pitting corrosion and galvanic corrosion vulnerabilities of the coatings. In the right application, the U.S. Navy could potentially use these coating materials in parts that are subjected to austere marine environments.

| **14. SUBJECT TERMS** cold spray, nanoparticle, dual, reinforcement | **15. NUMBER OF PAGES** 97 |
|---|---|
| | **16. PRICE CODE** |

| **17. SECURITY CLASSIFICATION OF REPORT** | **18. SECURITY CLASSIFICATION OF THIS PAGE** | **19. SECURITY CLASSIFICATION OF ABSTRACT** | **20. LIMITATION OF ABSTRACT** |
|---|---|---|---|
| Unclassified | Unclassified | Unclassified | UU |

NSN 7540-01-280-5500

Standard Form 298 (Rev. 2-89)
Prescribed by ANSI Std. 239-18

THIS PAGE INTENTIONALLY LEFT BLANK

**Approved for public release. Distribution is unlimited.**

# COLD SPRAYED COATINGS WITH DUAL NANOPARTICLE REINFORCEMENTS FOR WEAR AND CORROSION PROTECTION

Travis Norrell
Lieutenant, United States Navy
BS, University of Colorado, 2010

Submitted in partial fulfillment of the
requirements for the degree of

**MASTER OF SCIENCE IN MECHANICAL ENGINEERING**

from the

**NAVAL POSTGRADUATE SCHOOL**
**June 2020**

Approved by: Andy Nieto
Advisor

Troy Ansell
Second Reader

Garth V. Hobson
Chair, Department of Mechanical and Aerospace Engineering

THIS PAGE INTENTIONALLY LEFT BLANK

# ABSTRACT

As a form of additive manufacturing, the use of cold spray has made significant strides since different-sized particles were explored in the process. There is proof that micron-sized particles down to nanoparticles enhance the mechanical material properties of a substrate in wear resistance. Micron- and submicron-sized particles are beneficial, but due to their low relative surface areas, they tend to exhibit pull out more often and do not adhere to a substrate as well as a nanoparticle. Using nanoparticle metal and dual ceramic matrix reinforcements, six composites were fabricated through cryomilling and then applied to an aluminum substrate as a cold sprayed coating. Using nano-boron carbide ($nB_4C$) and boron nitride nanoplatelets (BNNP) at various combinations up to 2 vol%, an increase of 11.59% in hardness from the control was achieved. Wear testing of each coating was performed, but most of the tests drove through the coatings into the substrate, indicating more refinement of the testing parameters is required. Additionally, corrosion testing was performed on cold sprayed samples for 500- and 2,000-hr trials in a salt fog chamber, revealing underlying pitting corrosion and galvanic corrosion vulnerabilities of the coatings. In the right application, the U.S. Navy could potentially use these coating materials in parts that are subjected to austere marine environments.

THIS PAGE INTENTIONALLY LEFT BLANK

# TABLE OF CONTENTS

# LIST OF FIGURES

THIS PAGE INTENTIONALLY LEFT BLANK

# LIST OF TABLES

THIS PAGE INTENTIONALLY LEFT BLANK

# LIST OF ACRONYMS AND ABBREVIATIONS

| | |
|---|---|
| Al | Aluminum |
| $Al_2O_3$ | Aluminum Oxide |
| ARL | Army Research Laboratory |
| ASTM | American Society for Testing and Materials |
| $B_4C$ | boron carbide |
| BNNP | boron nitride nanoplatelets |
| CMC | ceramic matrix composite |
| CVD | chemical vapor deposition |
| DSC | differential scanning calorimetry |
| EDS | energy dispersive spectroscopy |
| GNP | graphene nanoplatelet |
| HEBM | high energy ball mill |
| HVOF | high-velocity oxygen fuel |
| MMC | metal matrix composite |
| NaCl | sodium chloride |
| PLA | polylactic acid |
| PVD | physical vapor deposition |
| SEM | scanning electron microscope |
| $Si_3N_4$ | silicon nitride |
| TEM | transmission electron microscope |
| XRD | x-ray diffraction |

THIS PAGE INTENTIONALLY LEFT BLANK

# ACKNOWLEDGMENTS

First, I would like to thank my thesis advisor, Andy Nieto, for the guidance and mentorship throughout this process. A thesis is a massive undertaking and it can be hard to know where to start or where to go, especially if you don't have a strong advisor. Andy, I thoroughly enjoyed all our discussions surrounding the thesis work and otherwise. I hope you stay at NPS a long time and work with as many thesis students as possible, because every one of them will be better off for it.

I would also like to thank my parents, Jim and Lorraine Norrell, for instilling a strong work ethic in me early and always being there for me. Whether things in life were going well or were more challenging, yours is the advice I've always turned to if I needed anything.

Finally, my wife, Elizabeth. You mean everything to me, and I know that you had to re-create yourself to come here to NPS with me. This was absolutely not the easiest path you could have taken, and I'm so glad you did. I'm stronger with you and can't wait to tackle everything else we have coming our way together.

THIS PAGE INTENTIONALLY LEFT BLANK

# I. INTRODUCTION

## A. MOTIVATION

Ships and the components onboard ships experience high degrees of stress from sea motion, operational loads, and frequent operational changes. As such, excessive component wear, protective coating deterioration, and complete mechanical failure is not uncommon. When this occurs, repair is based on a timeline that accounts for the degree of mission impact, availability of parts, and operational requirements. Often repair or replacement is limited by what personnel can perform locally. This can result in delaying repair or replacement of deficient components (sometimes for years) until operational requirements can support a shipyard maintenance period. For example, a crack in the superstructure of a forward deployed ship will wait until the ship no longer has operational commitments and is in a shipyard the following year to be fixed. Having degraded or broken components fosters an environment where personnel live with deficiencies and contributes to overall ship degradation. Therefore, providing the ship or unit with more tools to enable the repair of components on station is vital to supporting the overall Department of Defense mission. The primary objective of this thesis is to fabricate new ceramic particulate reinforced aluminum nanocomposite powders for use in cold spray that have enhanced hardness, wear, and corrosion properties over a pure aluminum powder. Furthermore, the thesis introduces two ceramic nanoparticles to the base aluminum powder to determine if there is a synergy between the particles further augmenting the aforementioned properties. Ideally, these composite materials will provide options for repairing or preemptively protecting engineering components throughout industry.

## B. CURRENT METHODS OF REPAIR/ENHANCEMENT

Frequently sailors use paint onboard ships to place a nonreactive barrier between bare metal and a corrosive at-sea environment. This is very helpful for reducing general corrosion, but paint can chip or delaminate, exposing a metal surface and resulting in localized corrosion if the exposed metal is not repainted. In addition, paint has minimal use for wear or impact

applications. In the event of high wear against a painted surface, the topcoat can easily be worn away, often requiring a reapplication of the paint coat.

Physical Vapor Deposition (PVD) and Chemical Vapor Deposition (CVD) are two methods of depositing coatings uniformly around a substrate within a closed environment. It is possible to obtain a high degree of controllability of thickness, including nanometric dimensions. It is understood that PVD and CVD have lower application rates when compared to other surface modification technologies and generally do not provide coatings as thick as some other treatments, like thermal spraying a large area with coatings over 100 μm [1]. While both of these coating methods can be easily performed in a lab environment with the right equipment, they are not as ideal for performing in-situ on a ship. Fully enclosing an installed part is usually not realistic and accessing tight spaces make either PVD or CVD less than an ideal choice for coating or repairing a component.

Plasma spray coatings use molten metal particles to impact a substrate, which then cool and solidify rapidly. High temperatures result in microstructure phase changes and subsequent residual stresses once the coatings cool down. These “quenching stresses” can result in tens of MPa residual stresses for ceramic reinforcements that can result in extensive splat cracking. In Matejicek’s study on stress evolution and mechanical properties of plasma sprayed coatings, an $Al_2O_3$ coating experienced this high quenching stress [2]. High residual stresses may affect the margin to yield stress that some other coating methods may not inherently produce because they do not reach the high temperatures resulting from plasma spray. In addition, plasma spray processes require temperatures in excess of 2000K for the particles in-flight [3]. On a ship where there is limited electrical power, this can unduly burden the turbine generators from the high-energy draw.

Cold spray is a low energy method that could be employed on ships to repair failed or degraded components and minimize the number of material deficiencies onboard the ship. When lead times for replacement parts are excessive (>12 months), a cold sprayed coating of the same or similar material could be applied to reduce down time and repair costs [4]. Additionally, cold spray can also be used to provide protective coatings to prevent material deterioration from corrosion or mechanical wear. In order to support the use of this

technology aboard ships, further research must be conducted to determine the mechanical properties and corrosion resistance of various application-compatible cold spray coatings.

Cold spray can be performed under a range of pressures, with high pressure normally resulting in a coating with better overall adhesion and a harder coating. Additionally, multiple reinforcements may have a synergistic effect, enhancing the properties of the base coating more than any one reinforcement alone. Starting with a high-pressure process would be a proof of concept for dual particle reinforcement, and future testing could closer simulate ship limitations and capabilities as a feasible possibility to repairing and manufacturing components. The possibility also exists for using these dual nanoparticle reinforcements as a coating onboard ships to strengthen components in a high stress environment prior to failure. There are multiple options for applying high strength coatings but having the additional ability to spray over complex shapes using quality powders or using a portable spraying device for large components would contribute to the crew's ability to repair parts in a timely fashion. Cold spray is one possible venue to explore to meet this objective.

## C. CORROSION CONSIDERATIONS

Cold sprayed coatings are inherently appealing for corrosion resistance, because they place a barrier between a substrate requiring protection and a potentially highly oxidizing environment. Ngai et al. [5]. analyzed the effects of saltwater corrosion on various cold sprayed samples, varying the carrier gas between helium (He) and nitrogen ($N_2$). Aluminum (Al) AA7075 powder was cold sprayed onto an AA7075 substrate. Both of the cold sprayed samples and a non-cold sprayed sample were then subjected to an immersion test and it was discovered that the bare substrate control experienced a relatively high degree of pitting in comparison to the cold sprayed samples. Specifically, the bare substrate experienced an average pit/pore ratio of 0.11±0.04 in a 0.1 $\frac{mol}{l}$ (M) NaCl solution and increased to a ratio of 0.26±0.16 in a 0.6 M NaCl solution. Using He as the carrier for a cold sprayed sample, the author saw a reduction in area ratio to 0.05±0.07 for the 0.1 M test and saw no increase at all for the 0.6 M test. This significant reduction in the number of pits may be correlated with a higher hardness of the cold sprayed coating, 158.8 HV vice 120.5 HV for the bare substrate [5]. The surface with a higher hardness may have experienced much less pitting because

there were fewer pores for corrosion to take place inside of and start the souring process associated with pitting. Even with the same grade aluminum as the base coating, a cold sprayed sample performed significantly better in an austere environment than the untreated aluminum because of the severe plastic deformation experienced in cold spray driving a denser microstructure less prone to pitting exposed to an oxidizing environment.

In the earlier corrosion example, the study explored the performance of a specific powder sprayed onto the same material in bar form and saw positive results. In other cases where the base material is highly susceptible to corrosion, cold spraying a less corrosive material can produce even more dramatic results. In the case of magnesium (Mg), one of the most anodic materials (-2.372 V vs. SHE [6]), applying a coating of any sort would potentially reduce the oxidation potential of the system. Diab et al. [7], applied a cold sprayed coating consisting of pure aluminum with an average particle size of 20 μm onto Mg alloy AZ31B and performed a salt fog chamber accelerated corrosion test over 33 days in accordance with ASTM B117. Over the 33 days the unsprayed, bare Mg alloy saw an average weight loss of 90%, compared to <10% average weight loss for the Al cold sprayed sample. Following a 90% weight loss, any material is rendered completely useless, creating the strong possibility for system failure. Weight loss reduction to under 10% is a significant change, and if an end-user requires using Mg or another metal with a high corrosion potential in a structural or load bearing application, a cold sprayed coating as in this example would make the application feasible.

## D. WHAT IS COLD SPRAY?

Cold spray is a form of additive manufacturing used to apply coatings at high velocities. Coatings are much more affordable than entire alloys and the largest benefit comes from the surface properties (in the case of this research, high wear and corrosion resistance). It typically uses a combination of metals and ceramics in powder form, usually a base metal with low amounts of ceramic reinforcements. In cold spray, there is no need to reach the melting point of feedstocks. Instead, high velocity causes plastic deformation that forces particles to adhere to the substrate. In nearly all research applications, cold spraying accelerates powder particles suspended in a supersonic gas flow to 300–1400 m/s using a

convergent-divergent de Laval nozzle [8]. Powder particles are driven by an inert gas (compressed air, nitrogen, or helium), accelerate as the cross-sectional area converges, reach the speed of sound within the throat of the nozzle, and then accelerate further in the divergent section once they are supersonic [9]. The high kinetic energy of the particles in the nanocomposite coating is used to deform the particles at impact with the substrate.

According to Raoelison et al. [9] the primary mechanism for the bonding between the cold sprayed coating and the substrate is intimate contact or by metallurgical bonding due to phase transformations. The coating particles experience a severe strain rate plastic deformation at the interface with the substrate. The excessive plastic deformation creates a high surface area contact that helps generate friction and keep the coating in place. There is no chemical reaction that would potentially impact the substrate or the bonding between the coating and the substrate.

Furthermore, temperatures in cold spray are much lower than in other coating technologies, allowing for lower energy consumption and are therefore inherently more appealing for shipboard use. The driving force is compressed air or an inert gas, usually helium, and no arc welding or plasma is needed. In High-Velocity Oxygen Fuel (HVOF) and plasma spraying, process temperatures near melting point of materials in use can often induce high levels of oxidation, porosity, chemical changes, and thermal stresses in the coatings. These all produce less than an ideal repair that may not provide a long-term solution onboard a ship or in another operational environment. Additionally, cold spray operations do not require extensive warm up times and are safer to work with than processes with excessively high temperatures.

The majority of cold spray machines are installed in a lab and can be relatively large in size. However, some cold spray apparatus can be smaller in scale and portable. This is more ideal for shipboard use than the large, lab-scale machines because it allows cold spray to be used in repairing or coating a component in-situ. Using this technology onboard ships may extend the life of some components under high stress due to the hard, cold sprayed composite taking the brunt of harsh conditions.

Cold sprayed coatings do not need the high temperatures that other thermal processes require. In the literature, the majority of cold spray runs can be performed between 100°C to 400°C [4]. The temperature of the feedstock is well below this temperature most of the time—this temperature refers to the gas propellant at the end of the heating elements in the nozzle. The feedstock powder is picked up in the hot flow, which causes its temperature to rise. Because of the supersonic speed of the gas, the process occurs very quickly, and the feedstock does not have time to reach high temperatures and does not stay at elevated temperatures long enough for a phase change to occur.

Helium is the preferred carrier gas for cold spray processes, as discussed by Gilmore et al. [10] and as shown in Figure 1. The mean particle velocity of copper powder in this figure was measured using a laser two-focus velocimeter along the spray axis. Helium has a lower density than compressed air and therefore exerts lower drag forces on the copper powder, resulting in higher particle velocities along the spray axis.

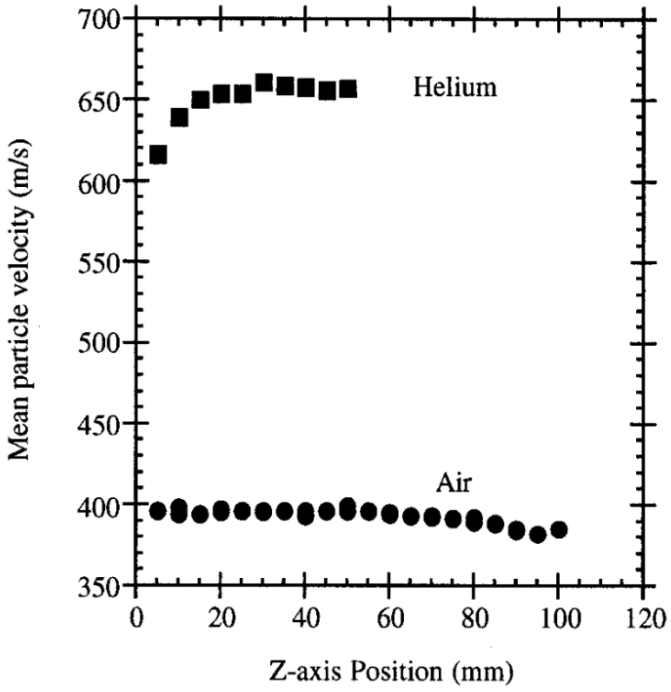


Figure 1. Velocity of Copper Powder Along the Spray Axis for Helium vs. Air as a Carrier Gas for a 2.1 MPa Cold Spray. Source: [10].

## E. AL-MMCS

It is well established that particulate-reinforced metal matrix composites (MMC) can exhibit wear resistance an order of magnitude higher than unreinforced materials under relatively low load [11]. This makes Al-MMCs in general not uniquely useful in a shipboard application, but across multiple industries. Aluminum is already a light metal with high strength, but reinforcing with an even lighter, stronger ceramic via cold spray has the potential to further increase strength and abrasion resistance when used in a coating application. One such ceramic, boron carbide ($B_4C$), is a strong ceramic reinforcement used in armor applications because of its exceptional physical and chemical properties, including a density of 2.52 g/cm$^3$ [12], a melting point of 2450°C, a hardness of 3700 HV [13], and elastic modulus of 445 GPa. In comparison, another ceramic reinforcement, aluminum oxide ($Al_2O_3$), has a density of 3.97 g/cm$^3$ [14], significantly higher making it less ideal than $B_4C$ for aerospace and other engineering applications because of its weight. Additionally, Thevenot discussed $B_4C$ having a high microscopic cross section for neutron absorption, making it useful in radiation shielding applications [12]. Tariq et al. [13] performed neutron attenuation tests for various thicknesses of $B_4C$/Al cold sprayed coatings and found that at least 50% of neutron radiation was attenuated with a 5 mm coating. While this example is a relatively thick coating, it shows the versatility of cold spray technology when paired with the right powders.

Nieto et al. [15] used various sized particle Al-$B_4C$ composites and found that nanoparticle ceramic reinforcements enhanced hardness more than their larger microparticle counterparts. Specifically, the Al-n$B_4C$ composite had a 56% higher hardness than unreinforced aluminum and 18% higher than Al-µ$B_4C$. This effect is driven by the high surface area to volume ratio inherent to nanoparticles, which increases exponentially going from the micro-scale to the nanoscale. Having an exceptionally high surface area drives a large surface energy of the nanoparticles to interact with the aluminum matrix and create more interfaces between the reinforcement and the matrix, thereby enhancing strengthening and increasing the hardness of the coating. Nieto et al. suggest that having a higher hardness reduced abrasive wear of the coating primarily by

reducing the penetration depth of the abrasive particles [15]. Not allowing the abrasive particles during the test to penetrate the coating as far would reduce the number of coating particles removed during the test and the overall mass loss of the coating.

Boron nitride nanoplatelets (BNNP) are another ceramic reinforcement but have a two-dimensional structure similar to graphene. It is well accepted they are exceptionally strong, having an elastic modulus of approximately 35 GPa [16]. They have a flat, disc-like geometry with a relatively large aspect ratio, making them useful in reinforcing applications. There is limited research in using BNNPs as a composite reinforcement for cold spray, but relevant comparisons can be made showing how useful BNNPs can be as a ceramic reinforcement in general. Lee et al. [17] used planetary ball-milling to mix a ceramic matrix composite (CMC) consisting of silicon nitride ($Si_3N_4$) reinforced with BNNPs and then consolidated the mixture by hot pressing. They found that the fracture toughness increased by 24.7% with only a 2 vol% BNNP and had a 9.4% increase in bending strength when compared to unreinforced $Si_3N_4$. Additionally, the author performed a wear resistance test and observed a drop in the coefficient of friction of 26.7% (0.38 to 0.30) with 2 vol % BNNP. In the study, BNNP was observed very minimally on the surface of the nanocomposite prior to the 39.2 N sliding wear test using Raman-mapping, but a significant amount of BNNP was observed on the surface following the wear test [17]. Considering significantly more BNNP was visible following the wear test is indicative that during the test, nanocomposite material was worn away consistently until more BNNP was exposed. At this point, the BNNP acted as a solid lubricant and arrested subsequent wear of the nanocomposite. BNNP is not limited to use within a CMC or hot-pressing consolidation and is promising to use in reinforcing aluminum for cold spray. Furthermore, studies have shown BNNP is chemically inert up to 950°C, compared to graphene oxidizing around 500°C, meaning that it may prove useful in high temperature applications as well [16]. In propulsion plants or other applications where pumps and bearings rely on lube oil for lubrication, a loss of lube oil casualty can be catastrophic. Once the lubrication film goes away, a bearing can be destroyed within seconds. Using solid lubricants like BNNPs in bearing materials can

provide operators precious time to assess and correct the casualty in these types of situations. Cold spray provides one venue to pursue consolidating these composites.

## F. PROCESSING OF MMCS

There are various techniques for processing MMCs. Two popular methods are high energy ball milling (HEBM) and cryomilling. HEBM uses various-sized milling balls to mechanically mix and deform materials within steel canisters. These canisters rotate vigorously around two separate axes, forcing the steel balls to impact the material within the canisters. This agitation thoroughly mixes materials and can also be used as a top-down approach to break apart materials until they reach the nanoscale. No chemical reactions take place, but temperatures do tend to rise in the canisters from friction generated between the milling balls and the materials. Figure 2 is a model generated by Feng et al. [18], to illustrate the interaction between the milling balls and powder within the steel canister during HEBM.

As the milling balls impact the powder or other material within HEBM, it causes distortion of the shape of the material and some particle size reduction. Impact between the powder and steel balls in HEBM also generates a large amount of heat energy. Li et al. [19] performed a differential scanning calorimetry (DSC) analysis on $TiB_2$/TiN high energy ball milling and estimated a maximum local temperature during milling of 300–500°C. These temperatures are not excessive but are a consideration when using nanoparticles. Particles on the nanoscale have a high amount of surface energy, and raising the temperature increases the potential for these particles to agglomerate. This agglomeration reduces the surface area to volume ratio and removes the primary reason for using nanoparticles to start.

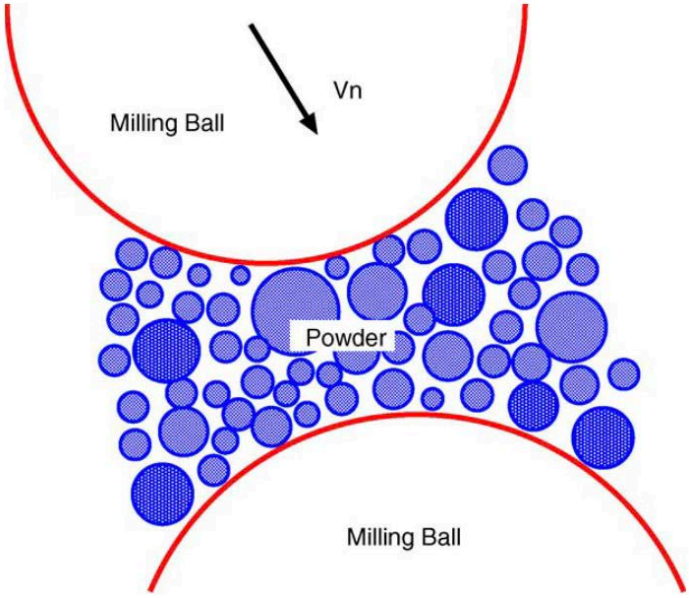


Figure 2. Visual Depiction of Interaction between Milling Balls and Powder in a HEBM Environment. Source: [18].

Cryomilling is another processing method for MMCs that promotes mixing and reduces the spacing between particles. Witkin and Lavernia discussed cryomilling also reducing the grain size throughout the sample [20]. Reducing the grain size is important to material properties because with a smaller average grain size there are more grain boundaries. These grain boundaries create more barriers for dislocations to traverse and prevent deformation of the material, increasing strength and hardness. In cryomilling, the sample and a milling media are loaded into a canister and then submerged in a bath of liquid nitrogen at -196°C. Once submerged and running, the mill uses mechanical agitation between the milling media and sample within the canister, mixing the sample and causing it to break apart. The interaction between the impactor and the sample is similar to HEBM except that any heat generated from the milling process is quickly dissipated in the liquid nitrogen bath. The cold temperatures prevent grain growth within the sample and also agglomeration or growth of nanoparticles. If performed for a long enough duration, cryomilling will reduce the overall particle size and distort the shape of the particles within the canister.

In the literature discussing cold spray applications, two important parameters that drive the collision and adhesion behavior of the particles are temperature and velocity [9]. Distorting the aluminum micro-particles makes them too aerodynamic, allowing the gas propellant to go around the particles rather than pick them up in the flow. This reduces the average particle velocity and therefore the adhesion/deposition efficiency of the cold spray process. Cryomilling is a particularly useful processing method because morphology of the particles remains largely unchanged when using low milling times while adequate mixing and some particle-size reduction takes place, as is discussed in the Chapter III. Low temperature (-196°C) of the liquid nitrogen environment helps ensure friction energy does not raise temperature too much, possibly reaching melting temperatures. As discussed in HEBM, nanoparticles in a high temperature environment agglomerate due to their high surface energy and lose the benefit of using nanoparticles in the first place. In addition, research shows low temperatures prevent recovery and recrystallization of powders and ensure chemical reactions between the powders are also avoided [11]. In any reaction, there is often an energy barrier to overcome for a reaction to take place and increasing temperature of the reactants can help overcome that energy barrier. The very low temperatures seen throughout cryomilling ensure these energy barriers are not overcome and no chemical reactions take place, therefore no grain growth occurs.

Comparing HEBM to cryomilling, Yandouzi et al. [11] performed an analysis of an aluminum-based matrix coating reinforced with $B_4C$ particles ranging from 1–14 μm in a cold spray application. The coating consisted of 20% $B_4C$ ceramic reinforcement and 80% spherical aluminum particles with diameter ranges from 5–65 μm. Notably, both the aluminum and $B_4C$ were larger than nanoscale in particle size. The author used either HEBM or cryomilling to synthesize various samples and then cold sprayed them onto an Al-Si substrate. The crux of the study was to compare how a ceramic reinforcement enhanced the wear properties of the composite coating cold sprayed onto the substrate. Yandouzi performed a wear test of the final product with a sliding distance of 200 m and saw a 66% wear resistance enhancement in the HEBM coating vs. the base aluminum coating. The sample that was cryomilled in coating preparation saw even less mass loss

[11]. This could be a result of the low temperatures used in cryomilling—high temperatures observed in ball milling may have caused a degradation of the composite material.

## G. DUAL NANOPARTICLE REINFORCEMENTS

An important part of this research involves exploring the effects of dual particle reinforcements, particularly when both reinforcements are nanoparticles. Polat et al. [21] reinforced an Al-Si matrix with various graphene and $B_4C$ mixtures, and received impressive results using a gas pressure infiltration consolidation method. Graphene is an allotrope of carbon, consisting of a single layer of atoms with a hexagonal arrangement of the atoms. In the study, Polat et al. used graphene nanoplatelets (GNPs) with an average thickness of 5–8 nm to coat the $B_4C$ reinforcement, which had an average particle size of 48 µm. The graphene had a much lower thickness than the overall size of the $B_4C$ and the high aspect ratio of the graphene ensured there was a large surface area for the $B_4C$ to adhere. With only 0.5 vol% graphene coating $B_4C$ within the matrix, Polat saw an increase in wear resistance by 55% and corrosion resistance by 12% compared to the unreinforced Al-Si matrix [21].

A contributing reason to the increase in wear resistance is that the GNPs act as a solid lubricant within the matrix. Berman et al. [22] observed that as the number of layers of graphene increase, the amount of friction generated in an atomic force microscopy tip-graphene interaction decreases. The author suggests that this is due to less out-of-plane deformation during the test resulting from increased van der Waals forces between the layers of graphene. The strong mechanical properties of GNPs combined with their plate-shaped structure reduces the friction coefficient of the composite matrix [22]. BNNPs have equally superior mechanical properties and share the same structure as GNPs, so they are expected to perform in the same manner when added to $B_4C$, possibly with a better resistance to high-temperature oxidation. Theoretically, BNNPs added to $nB_4C$ should provide a higher wear resistance compared to when added to $\mu B_4C$ because of the significantly higher surface area to volume ratio of $nB_4C$ when compared to $\mu B_4C$.

# II. MATERIALS AND EXPERIMENTAL PROCEDURES

## A. SELECTION OF MATERIALS

### 1. Commercially Pure Aluminum

For this study, a base material of commercially pure aluminum was chosen for the bulk material in the cold sprayed coating for its high resistance to corrosion. It is understood by other authors that compared to other materials that experience progressive oxidation resulting in rust and a loss of metal, aluminum develops a passive oxide layer that arrests corrosion early [23]. This makes it a good material to use from a corrosion standpoint, but it is still a very soft metal and is relatively weak compared to other metals, making ceramics a promising composite reinforcing material. Pure aluminum was used instead of an aluminum alloy that may contain other elements such as magnesium, silica, zinc, or iron because in the event of a chemical reaction between the aluminum and reinforcing elements, an alloy would make characterizing the reaction more difficult. Figure 3 depicts the general morphology and size of the base aluminum powder as shipped from the manufacturer using a scanning electron microscope (SEM). The aluminum powder has generally spherical morphology, making it ideal for cold spray. If the particles were flat and disc shaped for example, they would be more aerodynamic and would not get picked up in the flow of propellant gas during the cold spray process. Instead, the gas would pass over the particles and not drive them into the substrate at high enough speed to cause severe plastic deformation. The average particle size of the powder in Figure 3 is 27.4 μm.

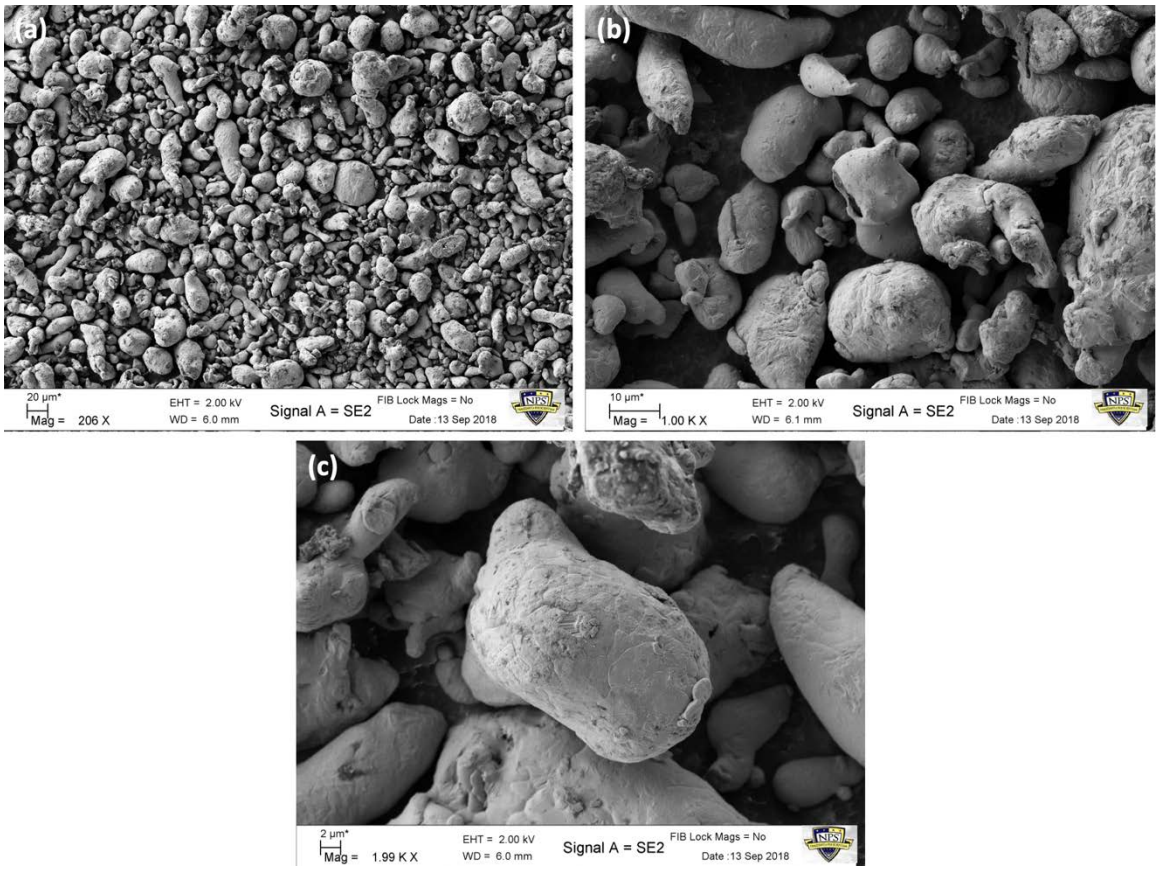


Figure 3. SEM Image of Commercially Pure Aluminum Used as Base Powder at (a) Low, (b) Intermediate, and (c) High Magnification

## 2. Reinforcing Ceramics

As discussed in the Introduction, boron carbide ($B_4C$) is a ceramic with an exceptionally high hardness and low density, making it ideal for a reinforcing application. Figure 4 shows a transmission electron microscope (TEM) image of the n$B_4C$ as shipped from the manufacturer. A TEM was required for adequate imaging of each individual particle of n$B_4C$ because of its small size, averaging less than 10 nm in diameter. The n$B_4C$ shown in Figure 4 is spherical similar to the base aluminum powder above.

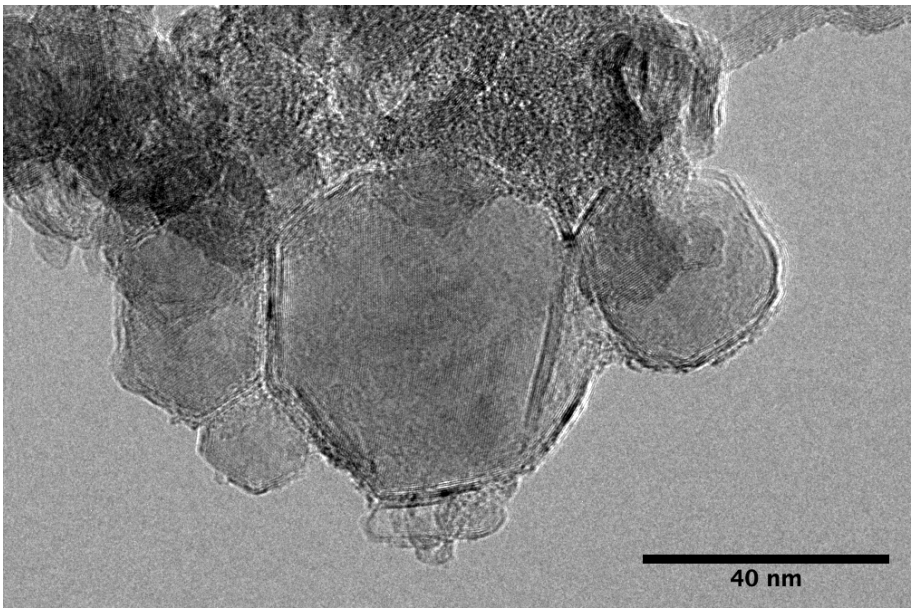


Figure 4. TEM Image of $B_4C$ Used as a Reinforcing Material

The second reinforcing material used for fabricating the composite powders is boron nitride nanoplatelets (BNNP). For this research, four different BNNP samples were considered, all with different size platelets and slightly different morphology between the four. Each of the samples, hereafter referred to as BN1, BN2, BN3, and BN4, were characterized using a dual beam SEM to determine which of the four would be the most useful for this research. The results are shown in Figure 5. BN1, BN2, and BN4 all have flaky, very flat morphology, with BN4 having the smallest average dimensions. BN2 appears to exhibit the most ductility between the three flaky BN samples as indicated by the bent ridges visible in Figure 5(b). BN3 depicts a thickness that is on the nanoscale but has a large aspect ratio when comparing the overall length of the platelets compared to the thickness. BN3 was selected for this research because of its large aspect ratio and because the platelets seemed to exhibit a ductile behavior the way they were folded around each other, typically not a behavior characteristic of ceramics. Ideally, the BN3 would increase the hardness of the composite material without making it overly brittle as a result of the morphology depicted in Figure 5(c). Figure 6 shows a TEM image of BN3. The red circle in Figure 6 is highlighting an area where the platelet is folded over itself similar to the platelets in Figure 5(c).

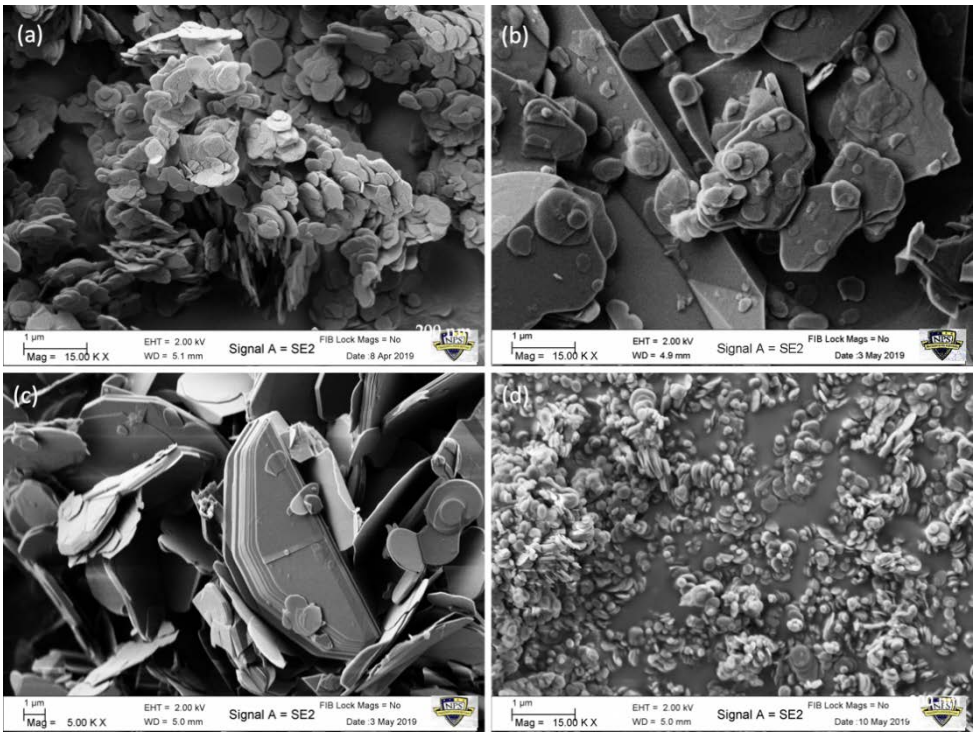


Figure 5. SEM Images of Four Different Samples of Boron Nitride Nanoplatelets (BNNP), (a) BN1, (b) BN2, (c) BN3, (d) BN4

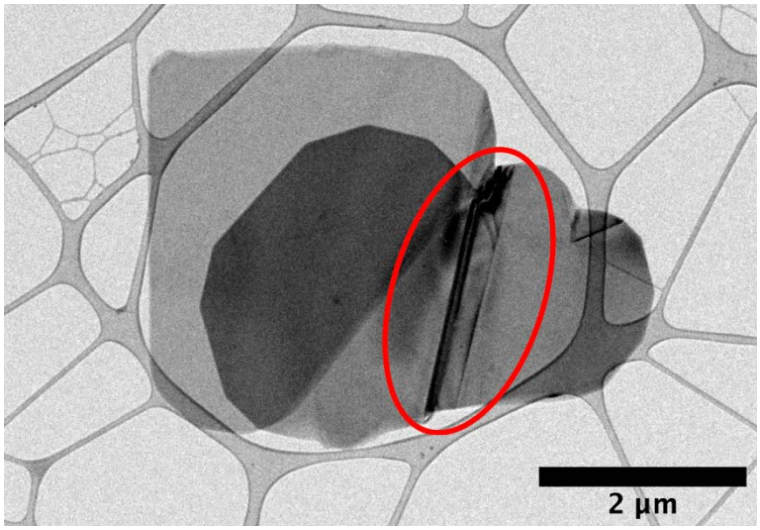


Figure 6. TEM Image of BN3 Used as Second Reinforcing Material. Red Circle Shows the BN Fold Over Itself, Indicating Relatively High Ductility

## B. EXPERIMENTAL METHODS

### 1. Synthesis and Summary of Coatings

Six samples were fabricated and studied; their compositions are listed in Table 1. To synthesize the coatings prior to cold spray, each of the samples were weighed and cryomilled using the Spex 6870 Freezer/Mill shown in Figure 7. All six coatings were cryomilled for five cycles, each cycle consisting of two minutes on followed by two minutes off. The two minutes spent off were an additional measure taken to ensure the temperature inside the sealed tube did not rise too high and result in agglomeration of the powder. If any of the nanoparticles had agglomerated together and grown in size, this would have removed one of the beneficial aspects for using nanoparticles in the first place - the high surface area to volume ratio driving a stronger composite matrix.

Table 1. Summary of Composite Coating Composition and Mixing

| Sample/Powder/ Coating | Mixture | Notes |
|---|---|---|
| 1 | 100 vol% Al | Control |
| 2 | 98 vol% Al<br>2 vol% $nB_4C$ | Cryomilled together |
| 3 | 98 vol% Al<br>2 vol% BNNP | Cryomilled together |
| 4 | 98 vol % Al<br>1 vol% $nB_4C$<br>1 vol % BNNP | All three cryomilled together |
| 5 | 98 vol % Al<br>1 vol% $nB_4C$<br>1 vol % BNNP | Al and $nB_4C$ cryomilled together, Al and BNNP cryomilled together, and then two resulting mixtures combined in HEBM w/o balls for two min |
| 6 | 98 vol% Al<br>1.67 vol% $nB_4C$<br>0.33 vol% BNNP | All three added together and then cryomilled |


Figure 7. Spex 6870 Freezer/Mill Shown (a) Closed and (b) Open with No Liquid Nitrogen

In coating 4, all three materials were roughly mixed together and then cryomilled. In coating 5, aluminum and $nB_4C$ were cryomilled together and then aluminum and BNNP were cryomilled together. Following the two individual cryomillings, the two mixtures were mixed a third time in a HEBM for two minutes without milling balls. Coating 4 was expected to demonstrate enhanced hardness and tribological properties over coating 5 because cryomilling the two ceramic reinforcements together would drive all of the particles closer together. Additionally, the difference between coatings 4 and 5 was expected to drive a higher standard deviation in hardness and tribological data for coating 5 because not all of the ceramic nanoparticles would be as evenly distributed using HEBM for final mixing.

Coating 6 contained five times more $nB_4C$ than BNNP by volume and was fabricated to determine if the excess $nB_4C$ would coat the higher surface area BNNP and result in any different behavior as a result. For this final coating, both of the ceramic nanoparticles were cryomilled together along with aluminum as in coating 4. Following cryomilling, each composition was passed through a 100 μm sieve to filter out any large particles.

## 2. Cold Spray Processing

In preparation for cold spraying, the AA6061 substrates were grit blasted with ~40 µm $Al_2O_3$ particulates. This sufficiently roughened the surface of the substrate so that the final cold sprayed coating would have better adhesion.

The cryomilled cold spray feedstock samples and prepared AA6061 substrates were then sent to the Army Research Lab (ARL) at the Aberdeen Proving Grounds in Maryland, where high-pressure cold spray application of each prepared feedstock onto the AA6061 substrate was conducted using the parameters listed in Table 2.

Table 2. Summary of Cold Spray Parameters

| | |
|---|---|
| **Gas Propellant** | Helium |
| **Pressure** | 3.447 MPa |
| **Temperature** | 425 °C |
| **Raster Velocity** | 200 mm/s |
| **Target Thickness of Coating** | 250 µm |

The stated parameters for the cold spray performed by ARL are state of the art. The driving pressure used at ARL, 3.447 MPa, is below the highest ranges of cold spray (up to 6 MPa [24]) but is well above the generally accepted definition of high-pressure applications of >2.0 MPa.

## 3. Corrosion Salt Fog Testing

After production of the six samples, an accelerated corrosion test was performed in accordance with ASTM B117 [25] using a large-scale salt fog chamber. Figure 8 shows the salt fog chamber in operation and Figure 9 shows the samples prior to conducting the corrosion test. The samples in Figure 9 are held in place by a polylactic acid (PLA) tray 3D printed for holding the samples during the corrosion test. The PLA tray held the samples at 20 degrees from the vertical and contained a drainage cavity below to prevent water buildup that could skew the results of the test. For the test, a 3.5% NaCl solution was used to simulate an austere marine environment. Two sets of samples were immersed in the chamber for testing - one set for 500 hours and one set for 2,000 hours. Quantitative

performance metrics were overall weight gain and thickness gain resulting from the formation of a passive oxide layer, measured weekly. Following the corrosion test, each sample was cut and characterized qualitatively using optical and electron microscopy.

Figure 8. Salt Fog Chamber in Operation

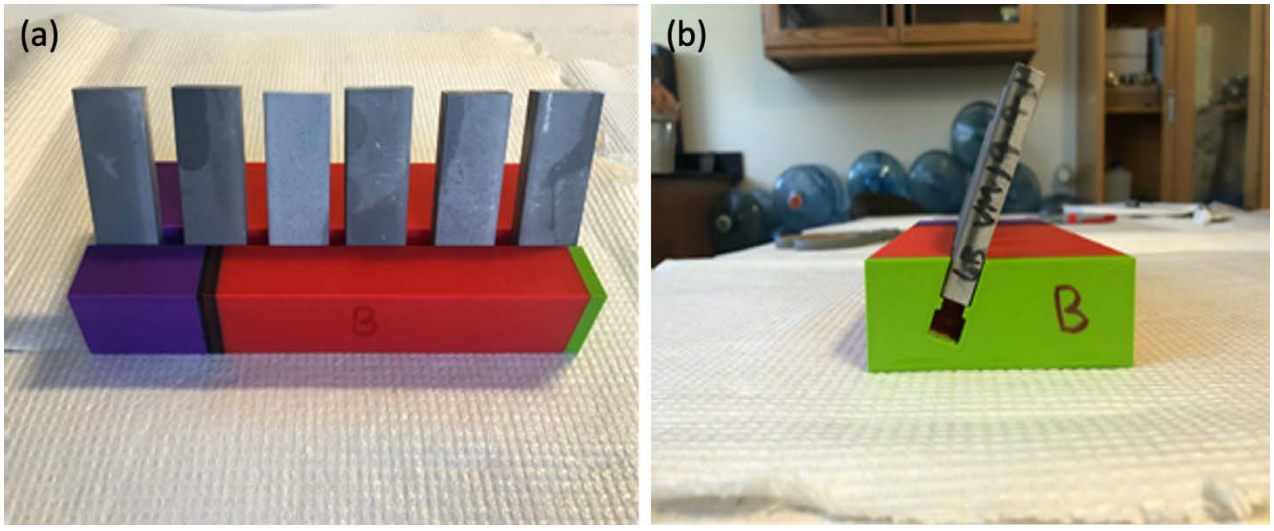


Figure 9. Front View and (b) Elevation of Cold Sprayed Samples Set in Holder Prior to Salt Fog Chamber Testing

## 4. Characterization Methods

### *a. Metallographic Preparation*

As sprayed samples and both sets of corrosion samples were sectioned and cold mounted in a SpeciFix resin and then cured over 24 hours, creating a sample puck. Each sample puck contained three samples each as illustrated in Figure 10. Each puck was grinded using 120-, 400-, 800-, 1200-grit paper and then finished using a 1 micron suspended alumina solution to better reflect light and increase contrast for microscopy.

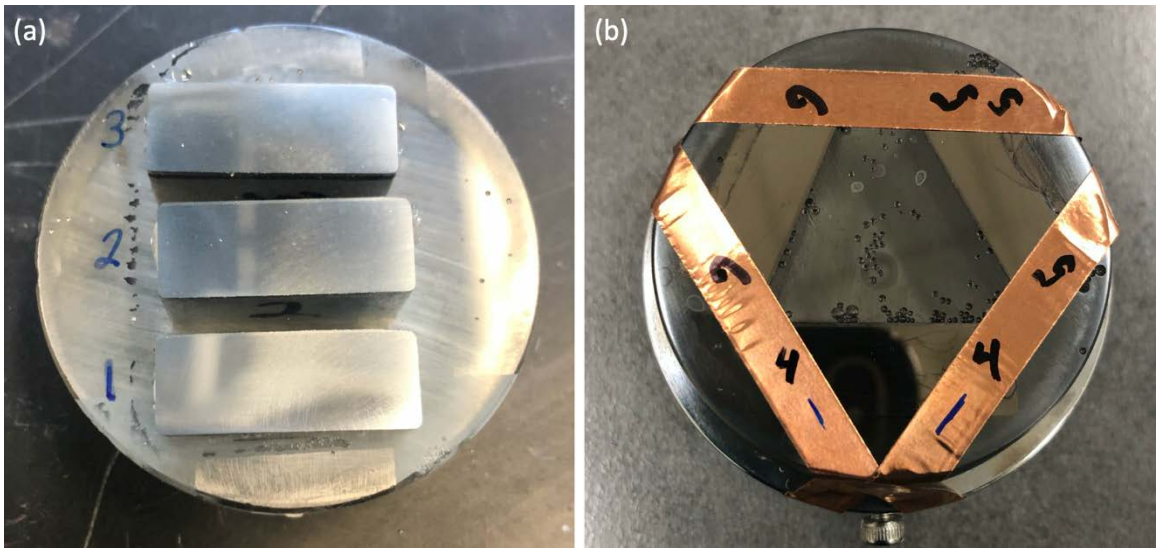


Figure 10. Polished Pucks Containing Three Coating Samples Each Following Grinding and Polishing

### *b. Microscopy*

Brightfield and darkfield optical imaging was performed using a Nikon Epiphot 200 optical microscope. For greater depth of field and higher magnification images, electron microscopy was performed using a Zeiss Neon 40 scanning electron microscope (SEM). Both of these microscopes were used for qualitative characterization of the as sprayed coatings and following corrosion and wear tests.

In order to prevent charging of the samples during SEM imaging, a Cressington 208HR sputter coater was used to coat each sample with a thin Pt/Pd layer that helped

minimize the buildup of electrons at any single point and saturate the surface. SEM imaging was performed using an accelerating voltage ranging from 2 kV to 20 kV at a working distance of 5 mm. The aperture was set to the standard 30 µm.

### *c. Microhardness*

A Struers DuraScan hardness tester was used to determine the hardness of each sample using series testing with a load of HV 0.1. Ten tests were performed for each coating in order to provide statistical significance between the coatings. The Struers DuraScan hardness tester creates an indent onto the material it is testing and uses the size of the indent to determine the hardness of a material. For a given load in the test, a smaller diamond indent will indicate a harder material because the sample does not plastically deform as severely compared to a larger indent.

### *d. Wear Testing*

A T50 tribometer was used to conduct ball-on-disk wear testing. Wear tests were conducted using 3 mm stainless steel balls as the counter-surface. A 10 N normal load was applied at a rotational speed of 200 RPM for 60 min. The track diameter was 6 mm and at least 2 tests were conducted for each composition. A second set of tests was conducted using a 5 N normal load and a 30 min run time. Wear volume measurements were conducted using depth profile data measured using a PS50 optical profilometer.

### *e. EDS Analysis*

An Energy Dispersive Spectroscopy (EDS) analysis was performed to determine the elemental composition in the vicinity of corrosion features in the cold sprayed coatings. The analysis was performed using the same SEM previously mentioned using an accelerating voltage of 20 kV and the high current setting turned on. The aperture was increased to 60 µm from the standard 30 µm to increase the electron current hitting the sample, thereby reducing the scan times. In EDS, a high-energy beam of electrons hits an atom within the sample and is absorbed, causing an electron within the atom to be ejected. Another electron in a higher energy state of the same atom subsequently drops down to fill the vacancy created. This second electron dropping energy levels emits an X-ray equal in

energy to the difference between the two energy states, and the energy of that X-ray is measured by a detector. The energy of this emitted X-ray is unique for every element, and performing a scan of an area in a sample can yield a high-resolution map of all the elements within the area.

### *f. XRD for Corrosion Samples*

A Rigaku MiniFlex 600 machine was used for X-ray diffraction (XRD) to determine which crystal structures were present within the coatings. The test was performed with an excitation voltage of 40kV and a current of 15 mA. The samples were cut to 2 mm thickness to be flush with the mount and aligned to maximize the incident area with the X-ray. XRD is fundamentally different from EDS in that X-rays are generated from a an anode within an X-ray generator. These X-rays hit the sample and diffract off of it for various angles with respect to the horizontal. The X-rays that cause constructive interference within the crystal lattice all reach the XRD detector and cause a peak in the signal detected. Every peak corresponds to a specific angle for which they were diffracted and the series of peaks generated by a sample are unique for every crystal structure.

THIS PAGE INTENTIONALLY LEFT BLANK

# III. RESULTS AND DISCUSSION

## A. COMPARISON OF HEBM AND CRYOMILLING

To determine which mixing method would be best suited to combine powder samples but not distort the spherical morphology of the aluminum matrix powder, a preliminary study was performed between HEBM and cryomilling. As previously discussed, both methods can be used for either a top down approach to create nanoparticles or as a method for thoroughly mixing two materials. In this research, the beginning reinforcing particles were already on the nanoscale and no further refinement of their size and shape was desired.

Lu et al. [26] looked at cycle times and the effects of both HEBM and cryomilling and found that both methods caused significant particle size reduction, especially within the first 15 minutes of processing. In this experiment, the authors analyzed the effects of both types of milling on a TiFe alloy cast with 4 wt% Zr. While milling BN was expected to produce different results than milling TiFe, the data from Lu's experiment helped set the baseline times for this research. The goal of the proceeding experiments was to determine which cycle times and milling methods would have the greatest effect on the BN to be used for cold sprayed coatings.

Multiple trials of both HEBM and cryomilling were performed on the same BNNP used in future cold spray runs. One trial was run for 10 minutes total, alternating two minutes on, two minutes off for five cycles. The second trial was run for 20 minutes total, alternating four minutes on, two minutes off for five cycles. The details of each trial are summarized in Table 3. All samples were characterized using an SEM and length measurements were taken using ImageJ software, taking no fewer than 200 measurements for particle length data. Figure 11 shows SEM images of the pre-cryomilled BN sample with an average length of 2.06 μm.

Table 3. Summary of HEBM and Cryomill Comparison Runs

| Machine | Mill Time per Cycle (min.) | Rest Time per Cycle (min.) | Number of Cycles | Total Mill Time (min.) |
|---|---|---|---|---|
| Cryomill | 2 | 2 | 5 | 10 |
| Cryomill | 4 | 2 | 5 | 20 |
| Ball mill | 2 | 2 | 5 | 10 |
| Ball mill | 4 | 2 | 5 | 20 |

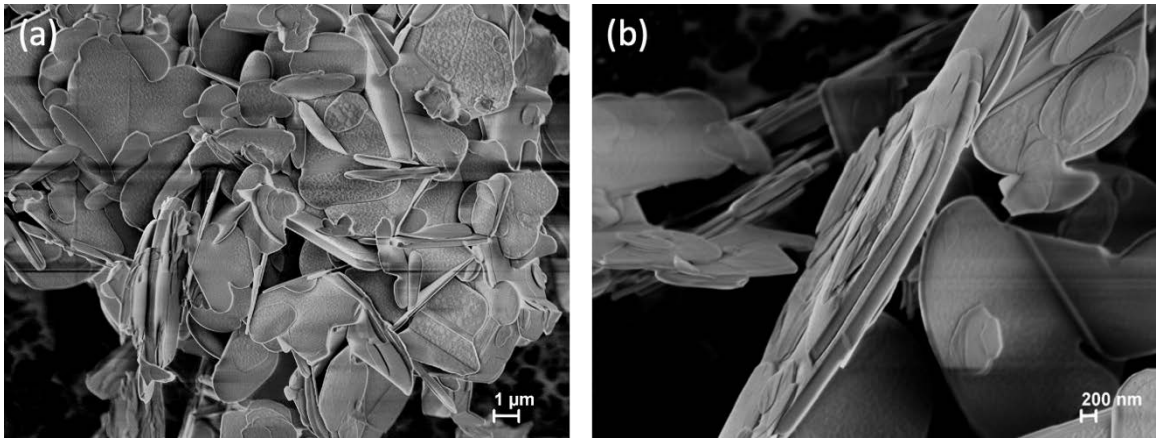


Figure 11. SEM Images of (a) Control BNNP (4-6 um lateral dimension) and (b) Cross-sectional View of Control BNNP

The results from both cryomilled samples are shown in Figure 12. The particle size distribution indicates that cryomilling for 10 minutes reduces the particle size and that cryomilling for 20 minutes reduces the particle size even further. Additionally, the size distribution appears to be narrower for 20 minutes of cryomilling than for 10 minutes. This is confirmed by a reduction of standard deviation from 1.31 µm to 0.58 µm. From visual observation, the general structure of the nanoplatelets is retained with a reduction in the lateral dimension.

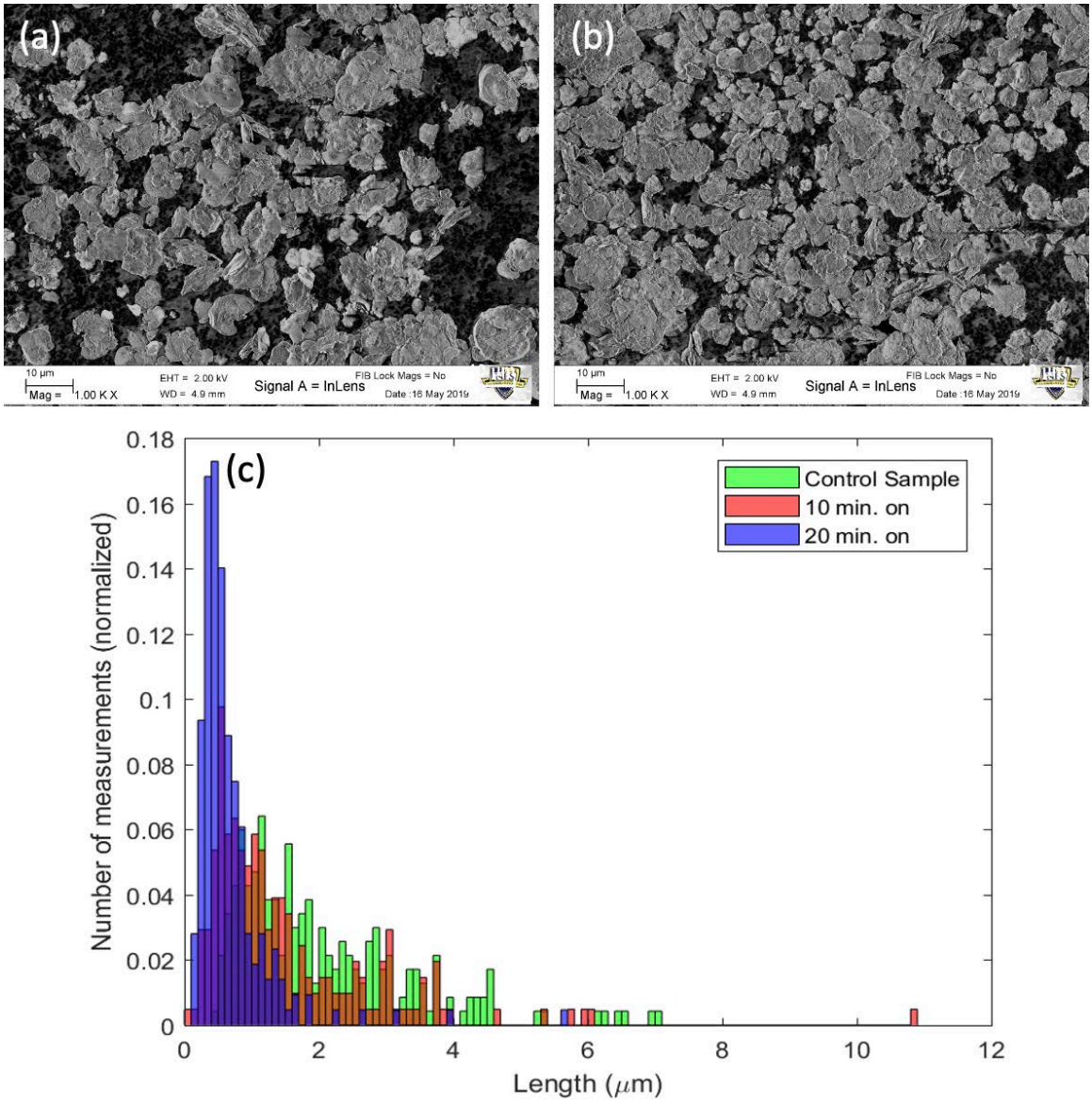


Figure 12. BNNP Following (a) 10 Minutes and (b) 20 Minutes of Cryomilling and (c) a Histogram of the Longest Dimension of BNNP in Each Group

Results from the two HEBM samples are displayed in Figure 13. The particle size distribution shown in the histogram indicates that ball milling increased particle size and broadens the distribution. Ball milling occurs at significantly higher temperatures than cryomilling which causes the nanoplatelets to agglomerate and lose the nanoscale dimension as shown previously in the control sample. Increasing the ball milling time increases particle agglomeration; average particle size increased from 7.25 μm to 8.78 μm.

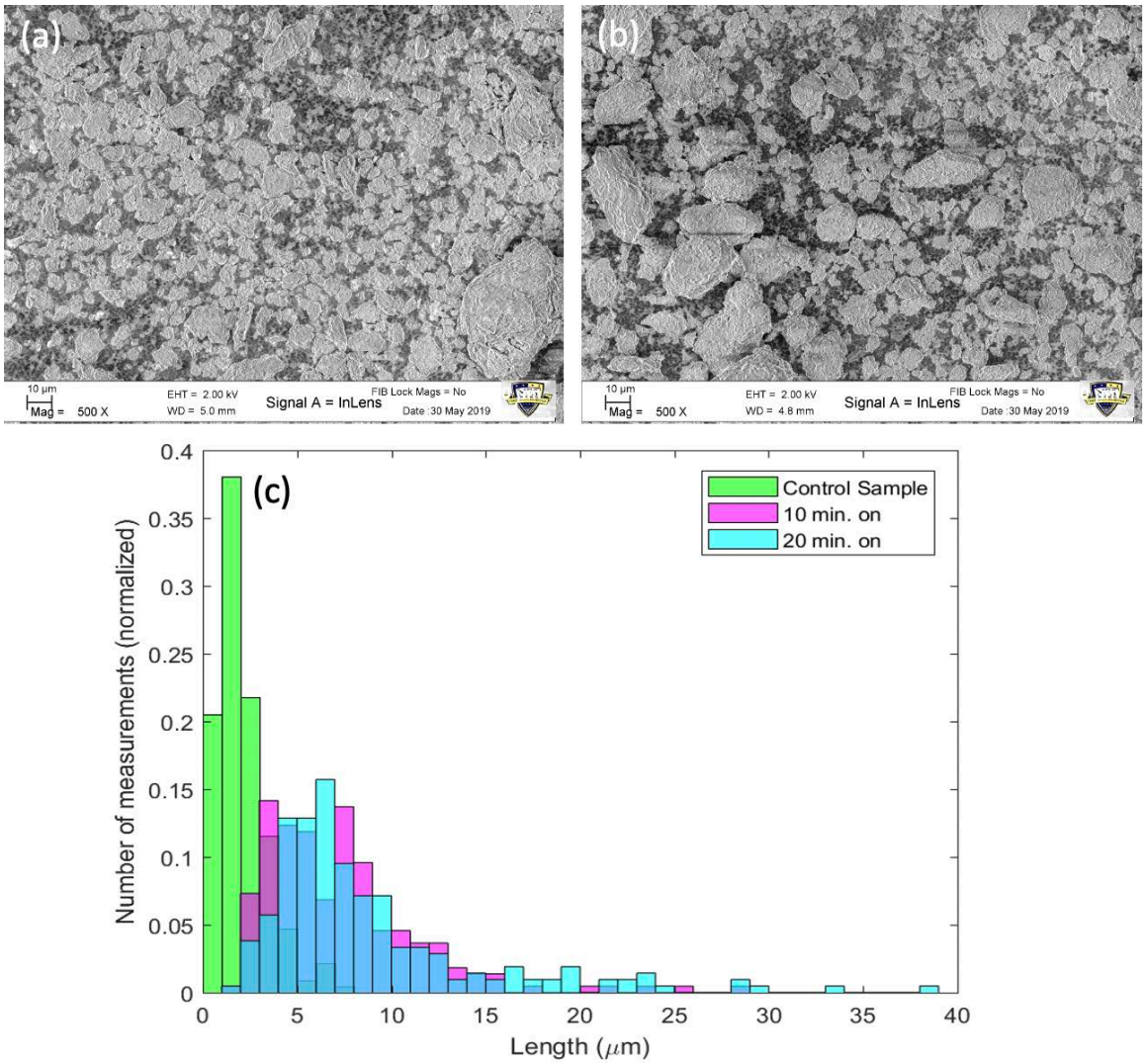


Figure 13. BNNP Following (a) 10 Minutes and (b) 20 Minutes of HEBM and (c) a Histogram of the Longest Dimension of BNNP in Each Group

Not only does ball milling cause agglomeration of the BNNP, but it can be seen from Figure 14(b) that the ball milling tends to destroy the platelet structure that provided a high aspect ratio that is beneficial in reinforcing applications. Evident in Figure 14(a), the cryomilling trials preserve the structure of the BNNP, nano scale on the thickness dimension with a large aspect ratio. Due to retaining the overall morphology of the BNNP as well as preventing agglomeration of the nanoparticles overall, cryomilling is determined to be a superior fabrication method over HEBM for the remainder of this research.

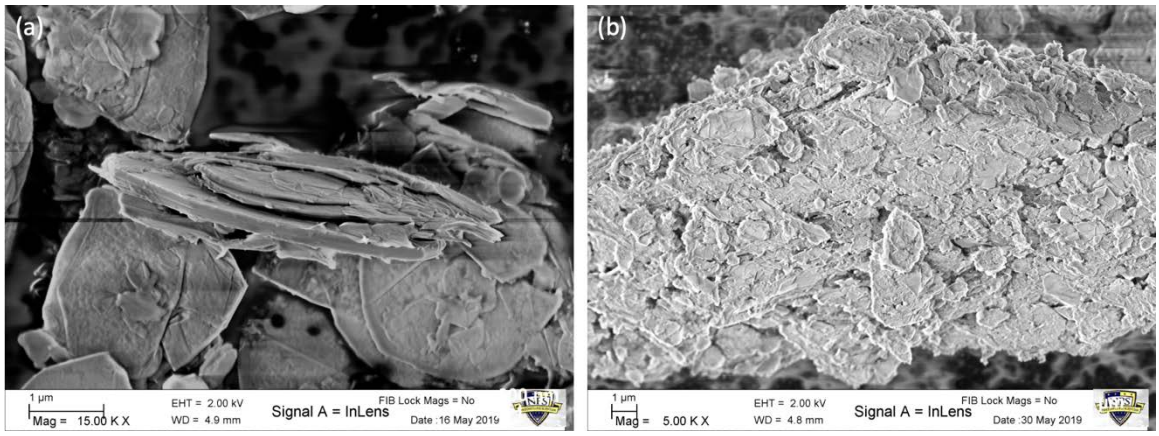


Figure 14. SEM Images of BNNP (a) Cryomilled for 20 Minutes and (b) HEBM for 20 Minutes

## B. CRYOMILLED ALUMINUM

In order to determine whether the aluminum used for cold spray would be distorted by cryomilling using the shorter duration run as with BNNP, aluminum was cryomilled alone for five cycles each consisting of two minutes on, two minutes off. The results are depicted in Figure 15. Both the spherical morphology and the average particle size appear to remain unchanged with a total of 10 minutes of cryomilling, indicating these run cycles are adequate for mixing the base powders without damaging any of them.

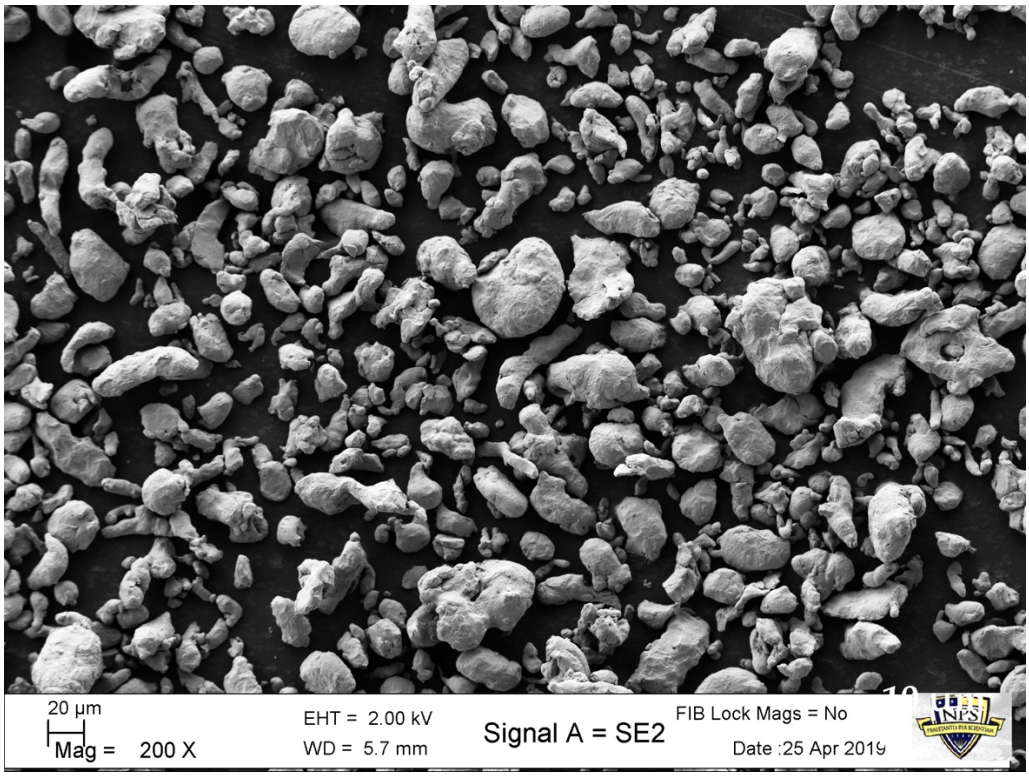


Figure 15. Aluminum Used for Cold Spray Cryomilled for a Total of 10 Minutes

## C. COMPOSITE POWDER SYNTHESIS

All powders were weighed and combined per the sample summary in Table 1. Figure 16 is an SEM image of coating 2, consisting of 98 vol% aluminum and 2 vol% $nB_4C$. The $nB_4C$ is coating the surface of the larger aluminum particles and has been sufficiently mixed by cryomilling. No chemical reactions have taken place between the two powders, and the $nB_4C$ is adhering to the large aluminum particles through van der Waals forces between the powders. Once the cold spray deposition took place, the individual splats were expected to experience severe plastic deformation at the surface of the AA6061 substrate and create a significant amount of dislocations within the splat due to the plastic deformation. Theoretically, the $nB_4C$ coating the surface of the aluminum would add to the number of interfaces created and serve as additional boundaries to diffusion on the atomic scale. This is referred to as dislocation pinning and would create a harder overall matrix. On the micro scale, individual splats would have a harder time

sliding past one another because of the increased roughness between the particles, also increasing the hardness of the matrix.

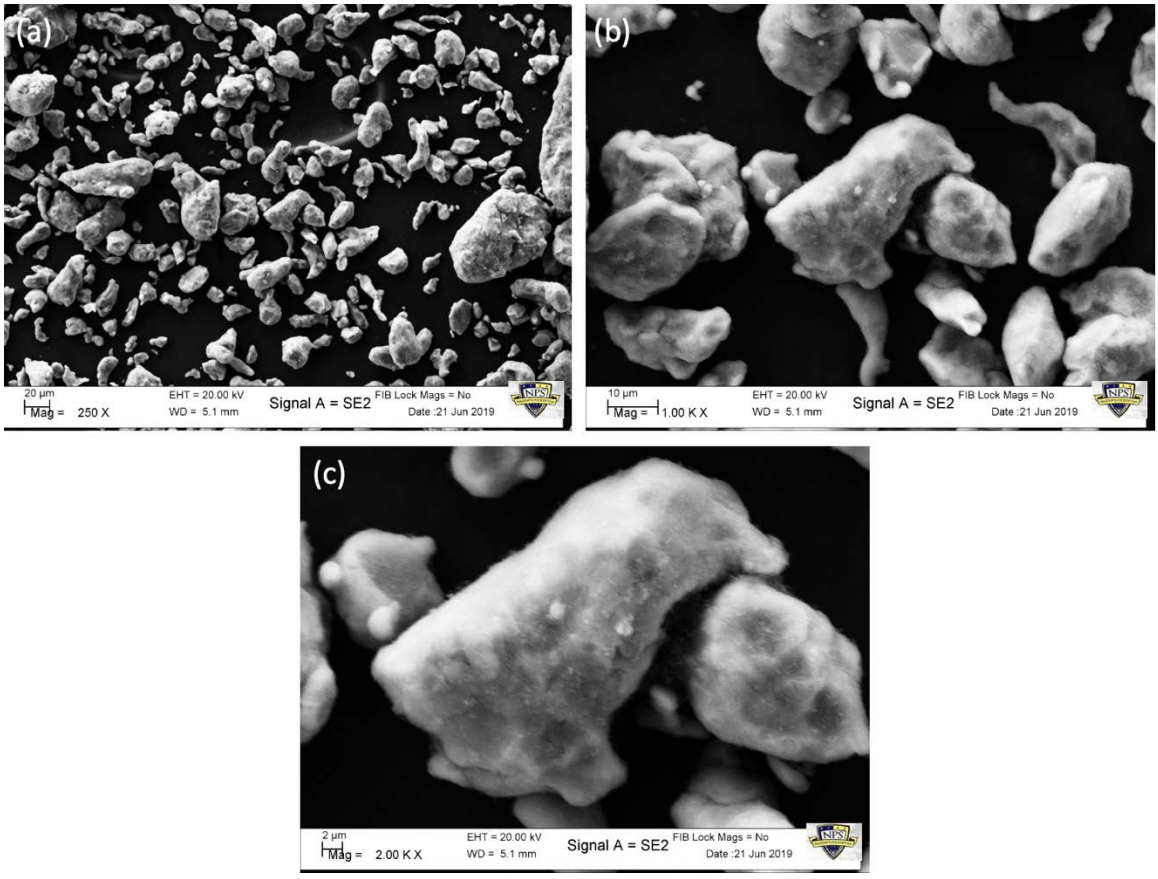


Figure 16. SEM Images of Aluminum and $nB_4C$ Cryomilled for 10 Minutes at (a) Low, (b) Intermediate, and (c) High Magnification

Powder 3 consists of 98 vol% aluminum and 2 vol% BNNP and is depicted in Figures 17 and 18 following cryomilling. In each image, the BNNP is indicated by red circles. It is clear that cryomilling again preserves the overall platelet structure of the BNNP and also thoroughly mixes the BNNP with aluminum. Also, van der Waals forces are still the dominant force maintaining the contact area between BNNP and aluminum. Because of their high aspect ratio, the BNNP does not coat the surface of the larger aluminum particles in the same manner as the $nB_4C$ in Figure 16. Despite lacking the degree of contact area as with $nB_4C$, the BNNP was still expected to cause a significantly higher

strengthening due its high aspect ratio. The high aspect ratio driving a high surface area was expected to endow the composite with more interfaces available for load transfer and therefore enhance dislocation pinning.

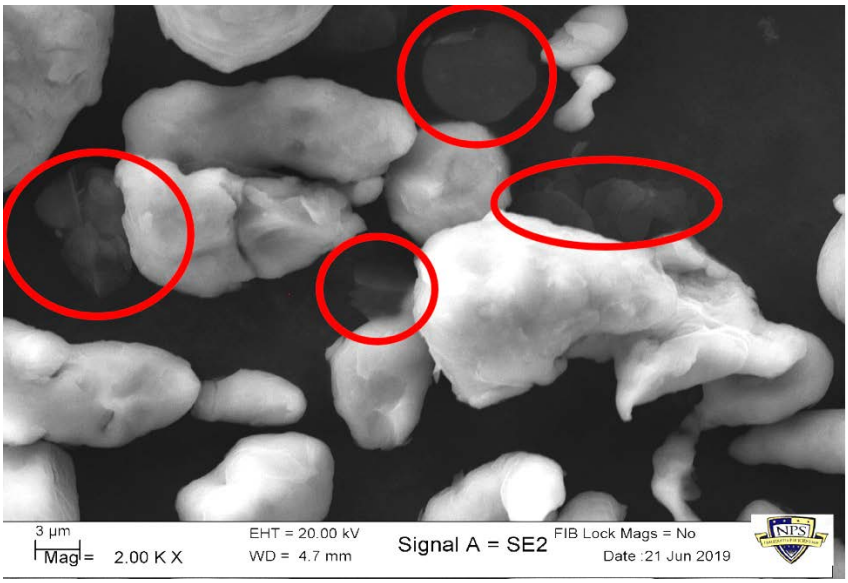


Figure 17. SEM Image of Aluminum and BNNP following Cryomilling at Intermediate Magnification - Red Circles Indicate BNNP

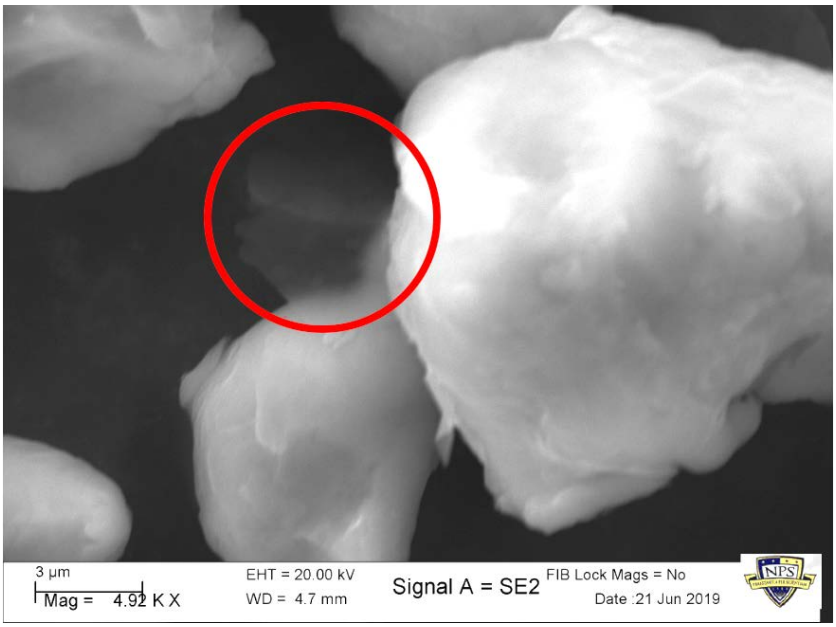


Figure 18. SEM Image of Aluminum and BNNP following Cryomilling at High Magnification

## D. VISUAL INSPECTION AND MICROSCOPY OF AS-SPRAYED SAMPLES

Visual inspection of each of the coatings upon receipt from ARL reveals a rough coating over the top of each surface. Figure 19 shows four of the six cold sprayed coatings upon receipt from ARL, all appearing nearly identical visually. After mounting and polishing cross sections of each sample, optical microscopy reveals a clear interface visible in each of the coatings, and there is no visible spherical morphology as with the base powders. The cold spray process causes sufficient plastic deformation of the powders to create very large surface area splats that adhere to the AA6061 substrate. No $nB_4C$ or BNNP is visible using optical microscopy, but it proves useful in measuring thicknesses of the coatings and performing low magnification comparisons. Table 4 quantifies the thickness of each as-sprayed coating using 20 different measurements for each coating.

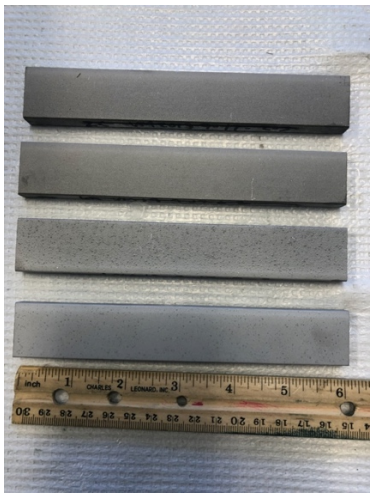

Figure 19. Four As-Sprayed Coatings Prior to Mechanical or Corrosion Testing

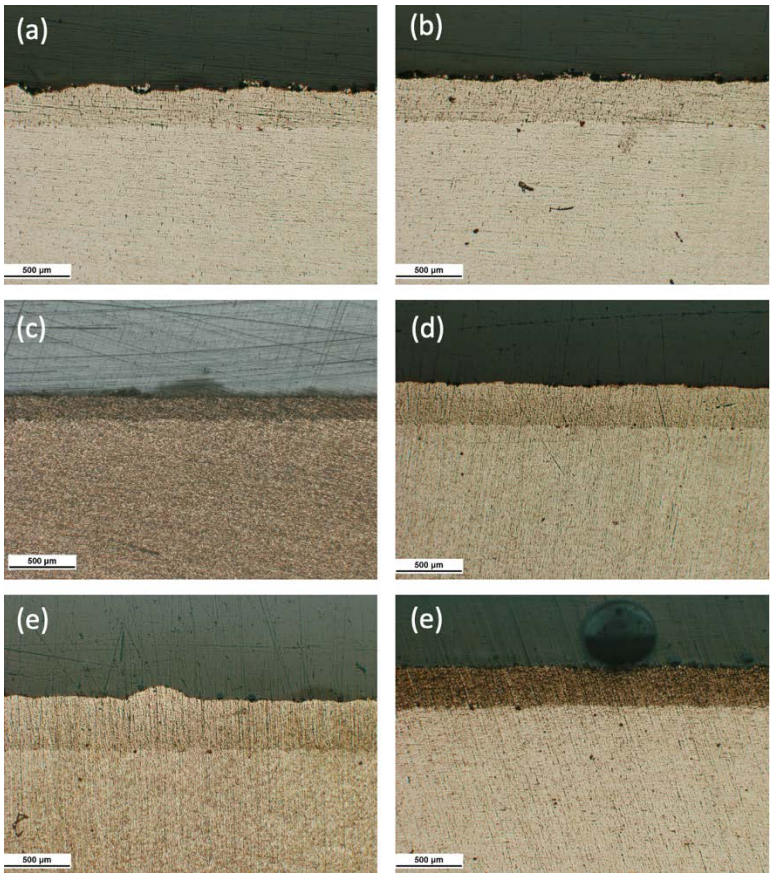


Figure 20. Optical Microscope Images of As-Sprayed (a) Al, (b) Al-2vol% $nB_4C$, (c) Al-2vol% BNNP, (d) Al-1vol% $nB_4C$-1vol% BNNP, (e) Al-1vol% $nB_4C$-1vol% BNNP (3 mixings), and (f) Al-1.66vol% $nB_4C$-0.33vol% BNNP Coatings

Table 4. Thickness Data for As-Sprayed Coatings

| | Coating 1 | Coating 2 | Coating 3 | Coating 4 | Coating 5 | Coating 6 |
|---|---|---|---|---|---|---|
| Average (μm) | 271.33 | 324.17 | 163.70 | 321.92 | 412.29 | 303.00 |
| SD (μm) | 24.58 | 15.84 | 10.07 | 16.55 | 38.64 | 16.11 |
| Min (μm) | 238.10 | 288.11 | 147.62 | 292.87 | 359.53 | 257.14 |
| Max (μm) | 328.57 | 347.63 | 176.21 | 342.89 | 495.26 | 326.20 |

Coating 3, which contains the highest volume percent BNNP, has a substantially thinner coating compared to the other five samples. Coatings 4 and 5 contain the second highest amounts of BNNP, but they do not have the second and third thinnest coatings, indicating that coating 3's relative thickness to the others is not a function of its BNNP content. To accurately determine whether the relative thickness of coating 3 is an anomaly that can be attributed to the cold spray method or if this is a result of its composition, more cold spray applications of that composition need to be performed. Coating 5 shows the thickest average but also has the highest standard deviation among the as-sprayed samples, 57.2% higher than the second highest standard deviation. The high variability of the thickness may be a result of the mixing process for that composition. Coating 5 contains 1 vol% of each reinforcing ceramic, but the two reinforcements were never cryomilled together. This mixing method was expected to increase the standard deviation of the hardness and tribological data, but it appears to have impacted the variability of the coating thickness as well. As with coating 3, a repeat of these cold sprayed applications would validate this result and would also further support cryomilling as a critical step in the powder mixing process.

No n$B_4C$ is observed within the cold spray coatings because of its small size compared to the aluminum and BNNP, but BNNP is observable in some instances. Figure 21 is an SEM image of BNNP within the cold sprayed coating lying flat on top of the cross section. The minute cracks throughout the two images and lighter colored circles are caused by sputtering the polished samples prior to characterizing with the SEM. It appears that the BNNP retains its shape from the cold spray process, making it more likely that it would assist in pinning dislocations and increase the overall hardness of the composite matrix.

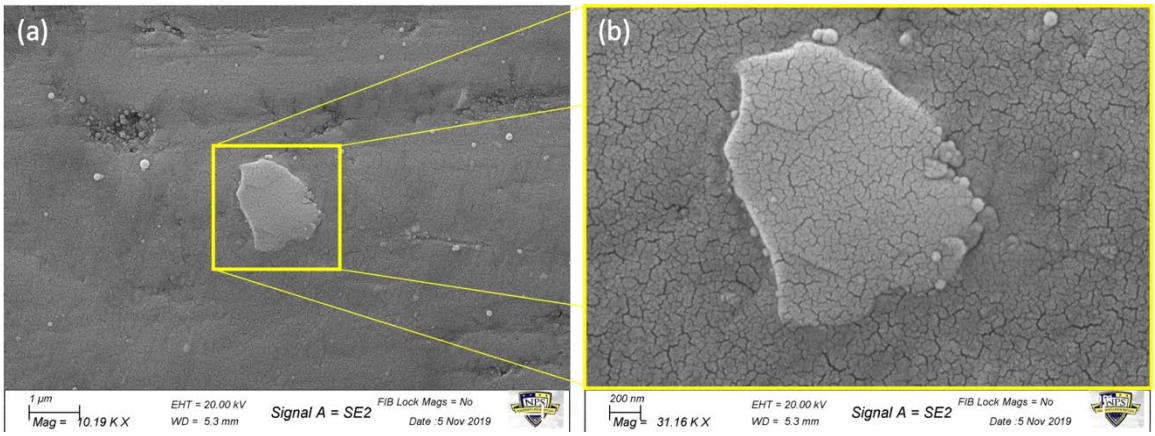


Figure 21. BNNP Observed in Coating 3 at (a) Intermediate Magnification and (b) High Magnification

## E. ETCHED SAMPLES

Powders within a cold sprayed coating experience a large degree of plastic deformation, retaining very little of their original shape. Instead, they create "splats" on the substrate and deposit as layers of splats on top of each other. Various coatings were etched using a HF-HCl-$HNO_3$ acid solution for 45 seconds to corrode the splat boundaries and reveal the splat shapes.

Figure 22 is a series of SEM images of Coating 1 etched at various magnifications, showing the splat boundaries revealed after etching. The splats are clearest in Figure 22(c) where there are two distinct splats - one on top of the other. During the cold spray application, a single particulate of feedstock powder impacts the surface of the substrate and plastically deforms at a high strain rate, creating a large surface area to adhere to the substrate. Almost immediately afterwards, a second particulate of feedstock powder impacts the first and plastically deforms as well. This creates the concave up half-moon shapes visible in Figure 22(c) and are representative of the layering process that occurs throughout the cold spray application.

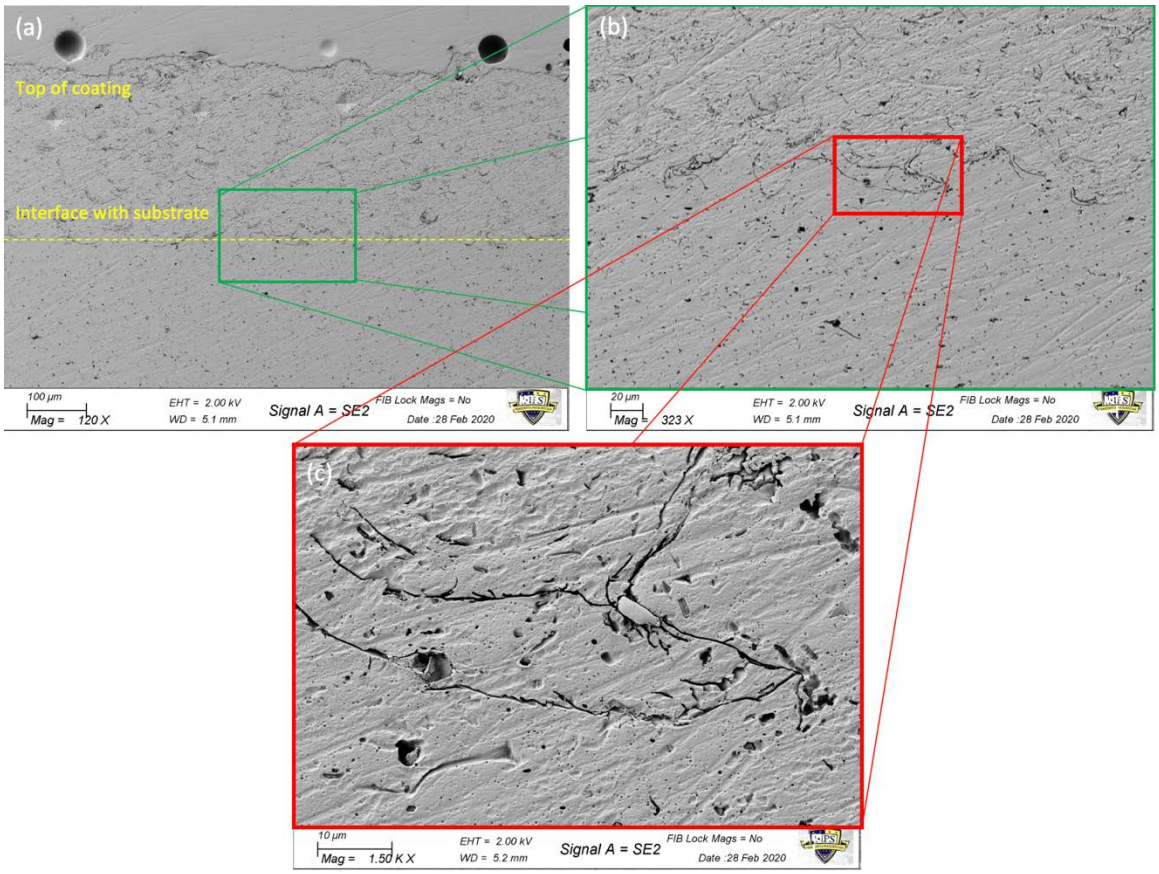


Figure 22. Coating 1 Showing (a) Low Magnification, (b) Intermediate Magnification, and (c) High Magnification of Etched Splats

Figure 23 is Coating 3 etched in the same fashion as Coating 1, showing many splats layered from the substrate through the bulk of the coating. Every one of the splats have the same concave up morphology as Coating 1, indicating that adding reinforcements does not impact the shape of the splats. Drawn in yellow in the middle of Figure 23 is the outline of a single splat which is representative of splats within each of the coatings. The caved-in shape on the top of the outlined splat is the result of another particle that impacts the splat on top at high velocity and deforms the splat further compared to its original deposition. This layering effect repeats itself vertically and horizontally throughout the coating. Figure 24 shows one of these splats for Coating 4 at higher magnification. Containing both BNNP and n$B_4C$, the splats in coating 4 look the same at those in Coatings 1 and 3, indicating again that changing the reinforcement contents at relatively low percentages does not change the shape of the cold sprayed splats. This is important because

maintaining the same shape of splats throughout multiple trials and different compositions will help with predictability of coating performance in future work.

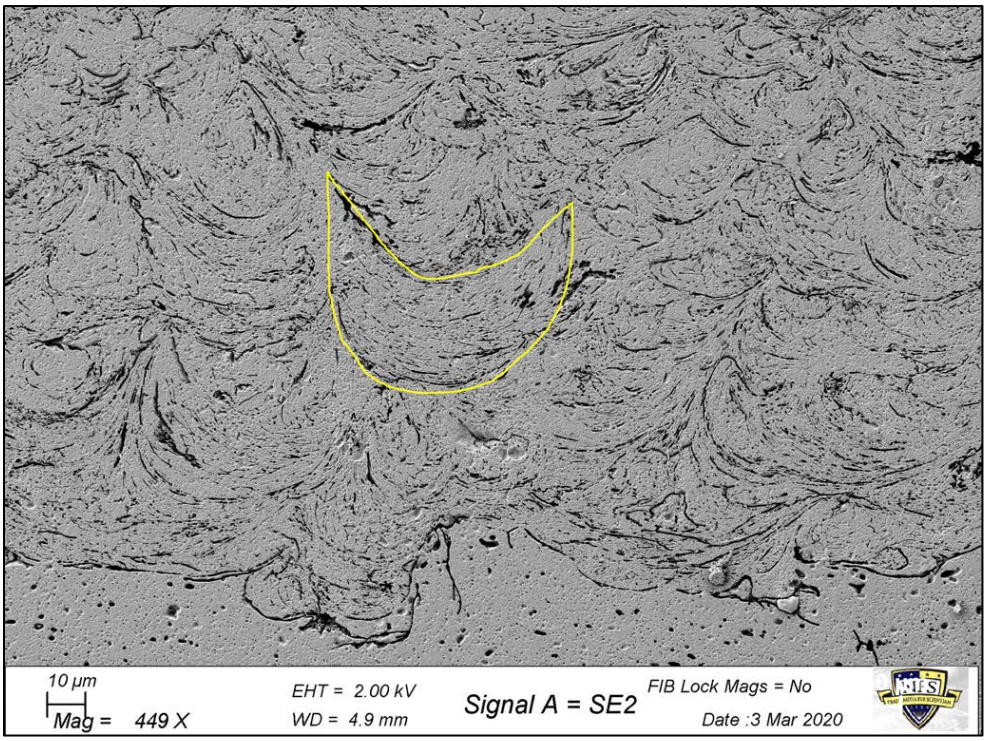


Figure 23. Coating 3 Etched, Showing Splats Layered Throughout the Coating

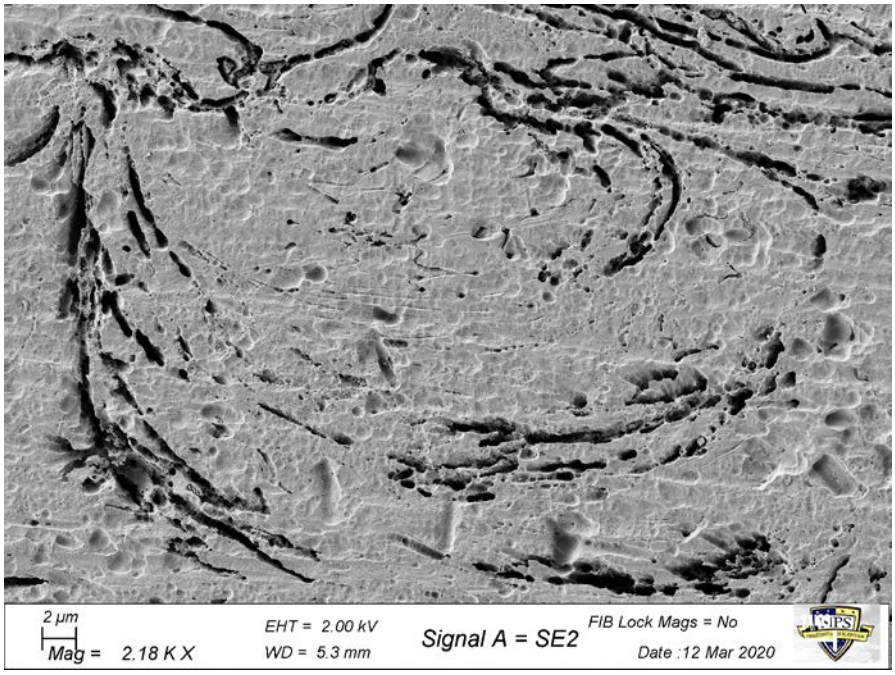


Figure 24. Coating 4 Etched, Showing a Single Splat

An intermediate and a high magnification image are depicted in Figure 25. It is difficult to definitively observe BNNP or nB$_4$C within a cold sprayed coating, but the flat platelet structure of BNNP is evident between splat boundaries in Figure 25(b). This entire region would have been more built up prior to etching, where the splat boundaries of the coating are preferentially corroded.

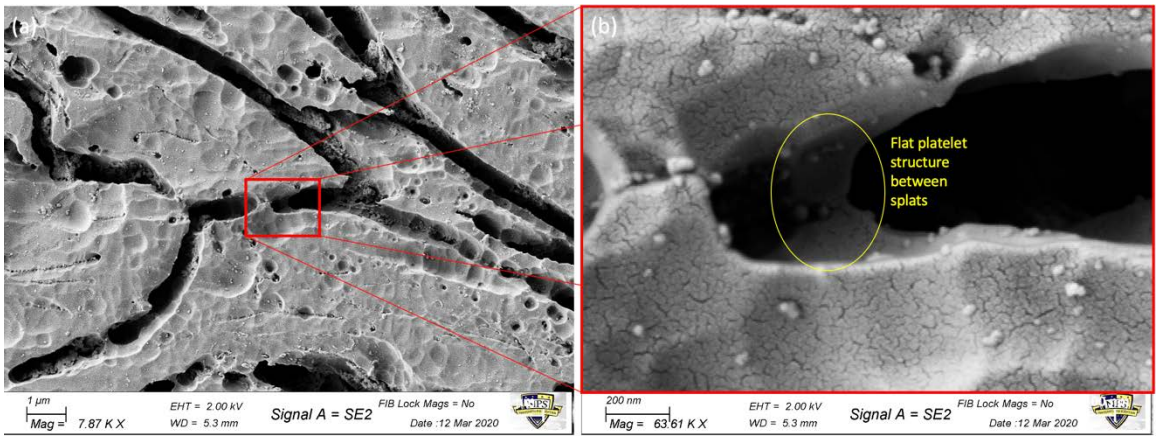


Figure 25. Coating 4 Etched at (a) Intermediate Magnification and (b) High Magnification, Showing a BNNP Between

## F. HARDNESS TESTING

Figure 26 shows an SEM image of the diamond shape indent representative of the indents made for every sample. The image depicts the control sample, coating 1, consisting of only aluminum. All of the hardness tests are taken in the middle of the coating, as indicated in Figure 26(a). There is a clear diamond shape in Figure 26(b), signifying a satisfactory test. On the outer portions of the indent, there is a buildup of material as the coating is pushed out of the way and plastically deforms during the hardness test. This indicates a relatively ductile behavior of the coating compared to coating 4 in Figure 24. Coating 4 consists of aluminum and 1 vol% each $nB_4C$ and BNNP to increase the hardness and wear performance of the coating. Comparing the indents made by the hardness test in the two figures, it appears that coating 4 in Figure 27 has a more brittle behavior as indicated by the lack of material building up at the outer portion of the indent. This more brittle behavior is generally associated with a harder composite matrix, making it appear qualitatively that adding $nB_4C$ and BNNP did in fact increase the hardness of the coating.

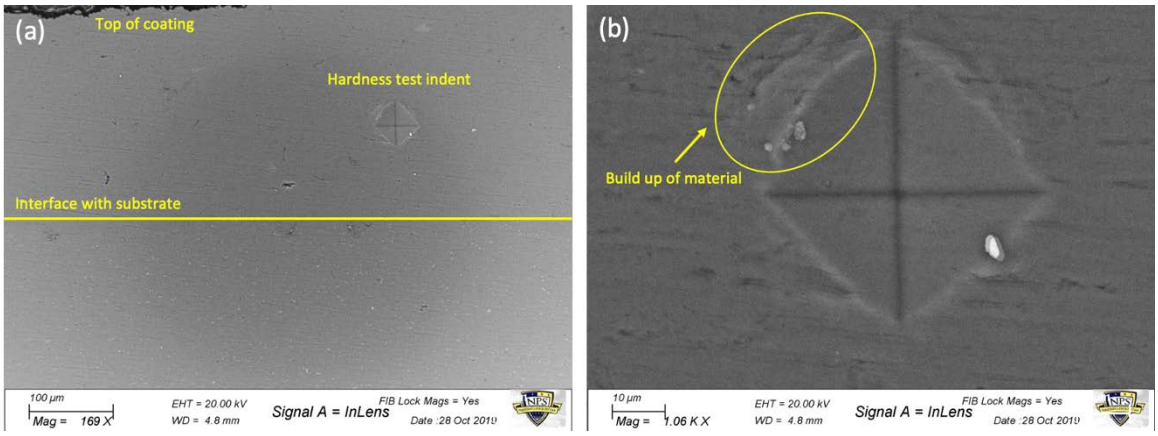


Figure 26. SEM Image of Coating 1 at (a) Low Magnification and (b) Intermediate Magnification

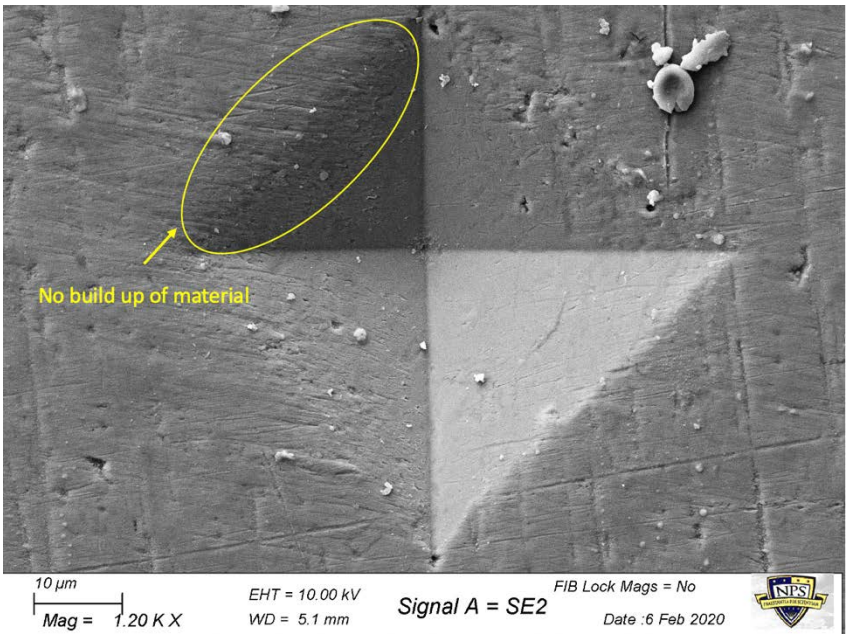


Figure 27. SEM Image of Coating 4 Showing a Relatively Brittle Behavior

For a quantitative comparison of the hardness testing between all of the coatings, Table 5 summarizes each one including the average Vickers Hardness (HV), standard deviation, and percent change from the control coating. It does not appear that adding $nB_4C$ alone (coating 2) provides any benefit with regards to achieving a harder matrix but adding BNNP alone (coating 3) does improve the hardness slightly. Of important note, all three coatings that contain dual reinforcement nanoparticles (coatings 4, 5, and 6) have improved hardness over the control and single reinforcement coatings, indicating a synergistic effect between the $nB_4C$ and BNNP when added to the same coatings. Specifically, coating 4 achieves a nearly 12% harder matrix with only 2 vol% total reinforcements - no more than any other coating. As with the coating thicknesses, coating 5 has the highest standard deviation from average. This is consistent with the requirement to cryomill the final powder composition together all at once in order to achieve the best mixing possible. Figure 28 graphically represents the average hardness between the coatings, with the standard deviation superimposed on the top of each bar. Each individual hardness test point for each coating can be found in Appendix A.

Table 5. Summary of Hardness Testing for As-Sprayed Coatings

| Coating | Average (HV) | Standard Deviation | % Change |
|---|---|---|---|
| 1 | 57.3 | 2.21 | 0.00 |
| 2 | 57.3 | 4.09 | 0.00 |
| 3 | 61.3 | 2.67 | 6.96 |
| 4 | 64.0 | 2.47 | 11.59 |
| 5 | 62.8 | 4.84 | 9.60 |
| 6 | 62.3 | 2.80 | 8.72 |

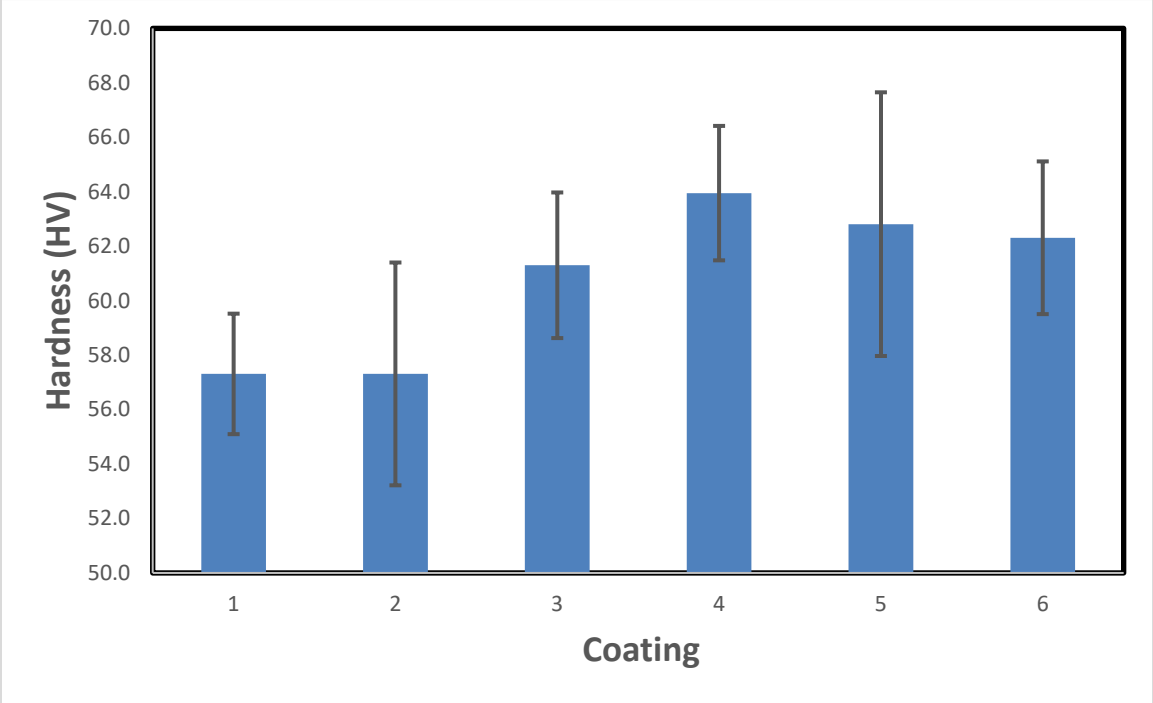


Figure 28. Graphical Representation of As-Sprayed Coating Hardness

## G. WEAR TESTING

Most of the wear tests wore away the entire thickness of the coating and proceeded to wear away the substrate as well. Considering the cold sprayed coatings are designed to protect the substrate, this did not prove that the ceramic reinforcements enhanced the wear properties of the composite coatings. It is possible that the two wear tests performed require further refinement of parameters to get conclusive data, however there are some valuable

insights. Figure 29 depicts the wear performance of coatings 1 through 5 under both 30 min and 60 min loads. Coating 6 is not shown in the graph because the wear damage was too extensive to be measured.

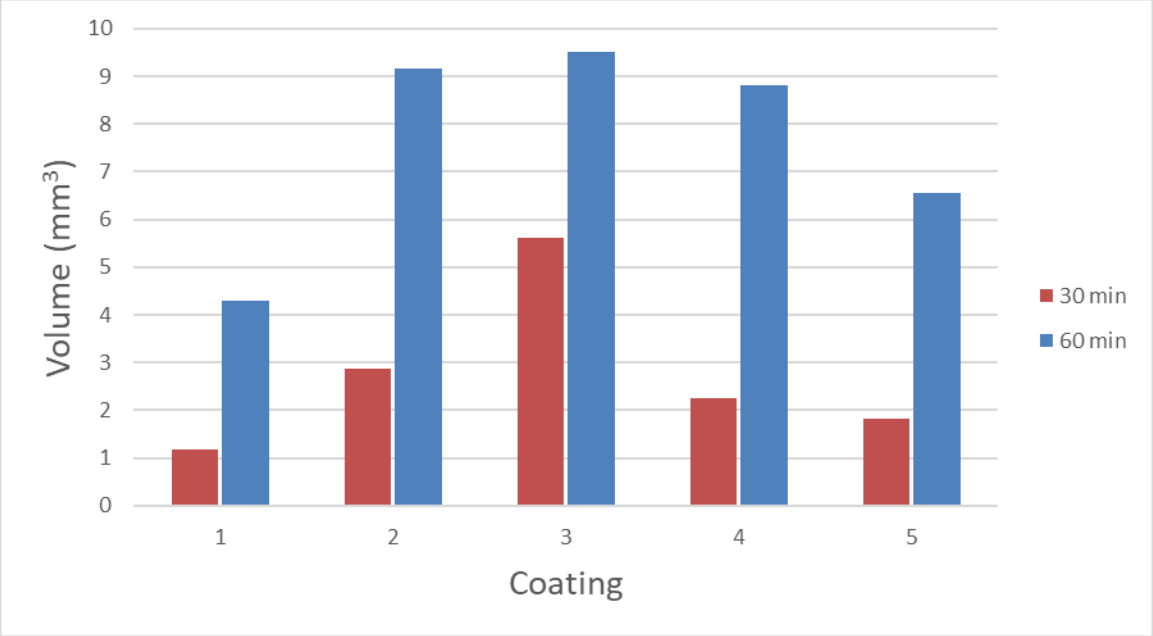


Figure 29. Wear Testing Data for Five Coatings for Both 30 Minute and 60 Minute Trials

It is clear from Figure 29 that doubling the amount of time and doubling the load applied during the wear test causes significantly more wear - approximately four times the wear volume for each of the coatings except for coating 3, which exhibits less than double the total wear. For coatings 1, 2, 4, and 5 this implies a linear relationship between the effects of loading time and loading force with wear volume that can be superimposed with each other. It is also possible that the relationship between these parameters is more complex and that loading force has significantly more impact on the results than loading time, for example. More tests while changing only one variable at a time are required to definitively assess any relationship between the stated parameters. Considering the tests traverse most of the coatings and wear away the substrate, it is also difficult to assess the

performance of strictly the coatings without the properties of the substrate impacting the results.

While all of the coatings perform poorly with regards to protecting the substrate, Coating 1 does exhibit the least amount of wear per Figure 29. This can be attributed to the relatively brittle behavior seen in Figure 27, where reinforcing ceramics are present. In a more brittle material response, pieces of the coating within the wear track would be more likely to fall away and create a larger wear volume seen in coatings 2 through 5.

An example of the profilometer output for one of the wear samples is depicted in Figure 30. The “Z Range” in Figure 30 refers to the depth of the profilometer reading, indicating that the maximum depth within the wear track is 399.1 µm. From Table 4, the average thickness of this coating is 271.33 µm and the maximum is 328.57 µm, so the profilometer is measuring at least 70 µm into the substrate in the darkest areas of the wear track. SEM images of the same coating in both a pristine, not worn section and also a section of the wear track are visible in Figure 31. In Figure 31(a), the surface is the uppermost layer of cold sprayed coating and is the last layer deposited during the application. The aluminum feedstock that plastically deforms and creates rounded-looking splats is visible. Figure 31(b) is an SEM image within the bottom of the wear track visible in Figure 30. It is clear that the steel ball counter surface that physically wore away the cold sprayed coating and substrate moved in a circular fashion, in some cases possibly pulling off pieces of the coating an revealing small holes within the wear track.

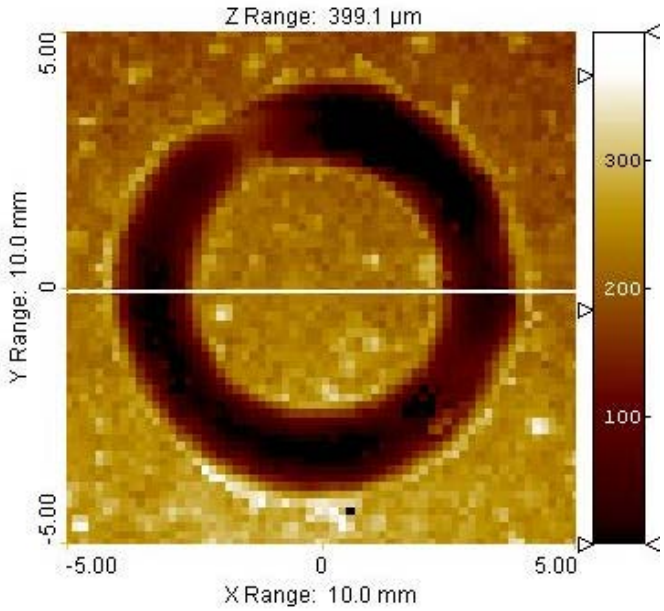


Figure 30. Profilometer Results of Coating 1

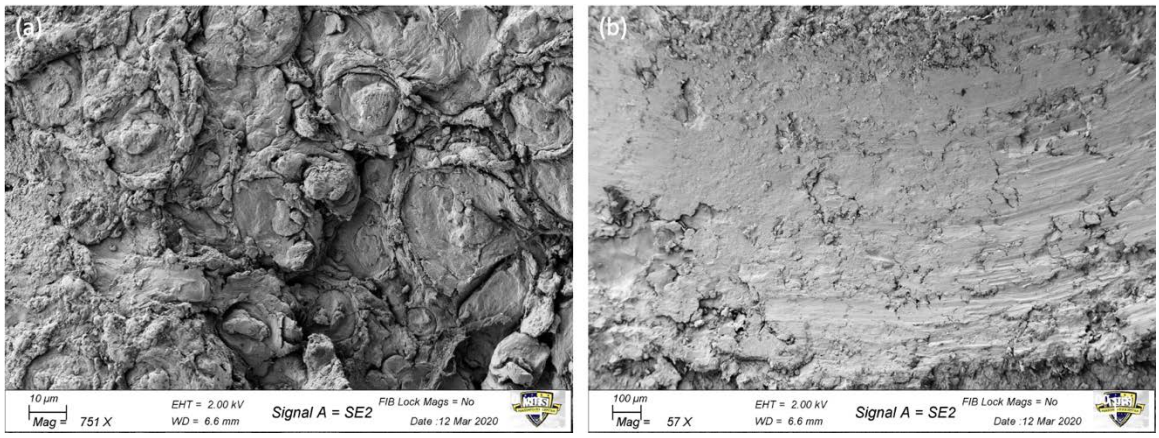


Figure 31. SEM Image of the Top of Coating 1 of a (a) Pristine and (b) Worn Area

## H. CORROSION TESTING

### 1. 500-Hour Samples

#### *a. Pitting Corrosion Characterization*

Following the salt fog chamber testing, the first test performed was a visual inspection of each sample. Because of the salt residue present on the surface of each

sample, it is likely that each one had experienced some degree of corrosion - NaCl would have provided a reliable source of chlorides to corrode the metal. Figure 32 shows each one of the samples following 500 hours in the salt fog chamber.

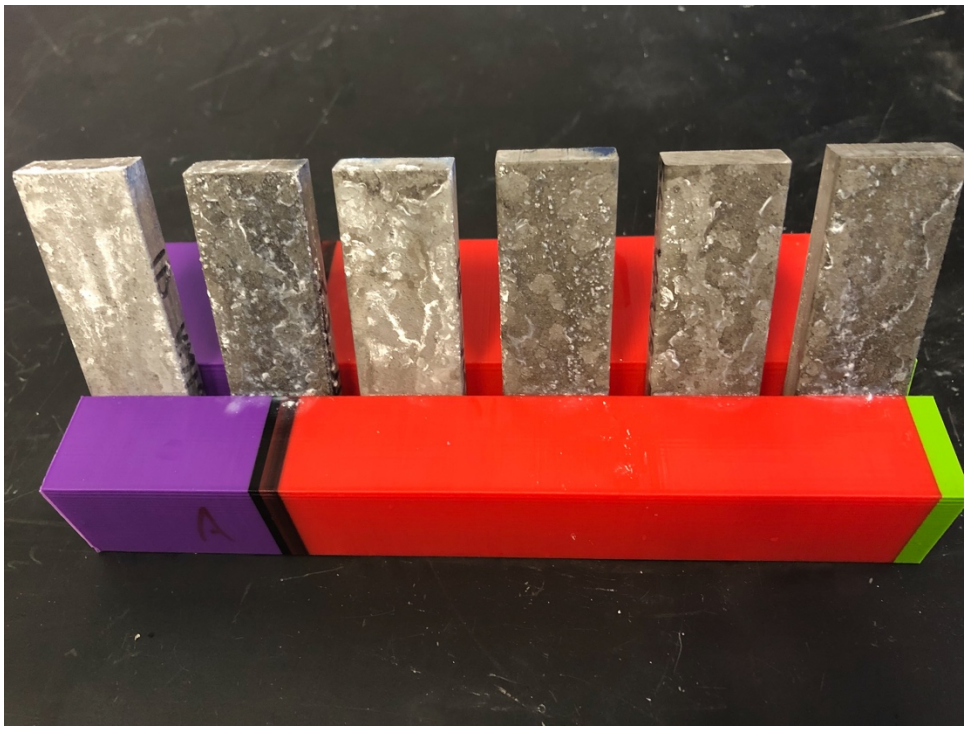

Figure 32. Sample Coatings in Order 1 Through 6, from Left to Right, Following 500 Hours in a Salt Fog Chamber Accelerated Corrosion Test

Coating 1 (control) performs the best by all metrics analyzed. Table 6 shows the thickness and weight values for four different times throughout the 500-hour test. Every sample exhibits an increase in mass and thickness, indicating an oxide layer forming on the surface of the coating. Oxide layers create an area of passivity and greatly reduce the amount of corrosion that occurs on a surface, and the mass gain and thickness gain is indicative of how much of a passive oxide layer is formed. While an oxide layer is protective in nature, it still represents a loss of material on the surface and corrosion of the exposed layer. Coating 2 exhibits the highest mass gain and thickness gain from all of the samples, indicating the worst corrosion performance from a quantitative perspective.

Table 6. (a) Mass and (b) Thickness Measurements Over Time for 500-hour Samples

| (a) | 0 hours (initial) | 168 hours | 336 hours | 504 hours | Change from initial |
|---|---|---|---|---|---|
| Sample | Mass (g) | | | | |
| 1 | 44.33 | 44.37 | 44.47 | 44.43 | +0.10 |
| 2 | 43.91 | 44.15 | 44.23 | 44.26 | +0.35 |
| 3 | 42.98 | 43.02 | 43.11 | 43.10 | +0.12 |
| 4 | 44.60 | 44.74 | 44.79 | 44.72 | +0.12 |
| 5 | 44.16 | 44.32 | 44.32 | 44.25 | +0.09 |
| 6 | 43.96 | 44.20 | 44.22 | 44.18 | +0.22 |

| (b) | 0 hours (initial) | 168 hours | 336 hours | 504 hours | Change from initial |
|---|---|---|---|---|---|
| Sample | Thickness (mm) | | | | |
| 1 | 9.7 | 9.8 | 9.9 | 9.8 | +0.1 |
| 2 | 9.7 | 10.0 | 10.1 | 10.1 | +0.4 |
| 3 | 9.7 | 9.7 | 9.8 | 9.8 | +0.1 |
| 4 | 9.7 | 9.9 | 9.9 | 9.9 | +0.2 |
| 5 | 9.9 | 9.9 | 10.1 | 10.0 | +0.1 |
| 6 | 9.7 | 9.9 | 10.1 | 9.9 | +0.2 |

Figure 33 shows brightfield optical images from all six coatings taken at 25X magnification. On the lower half of each picture, the substrate is brightest part of the images with a darker, thinner portion above representing the cold spray coating. The upper portion of each image is the puck epoxy that was used to mount each sample.

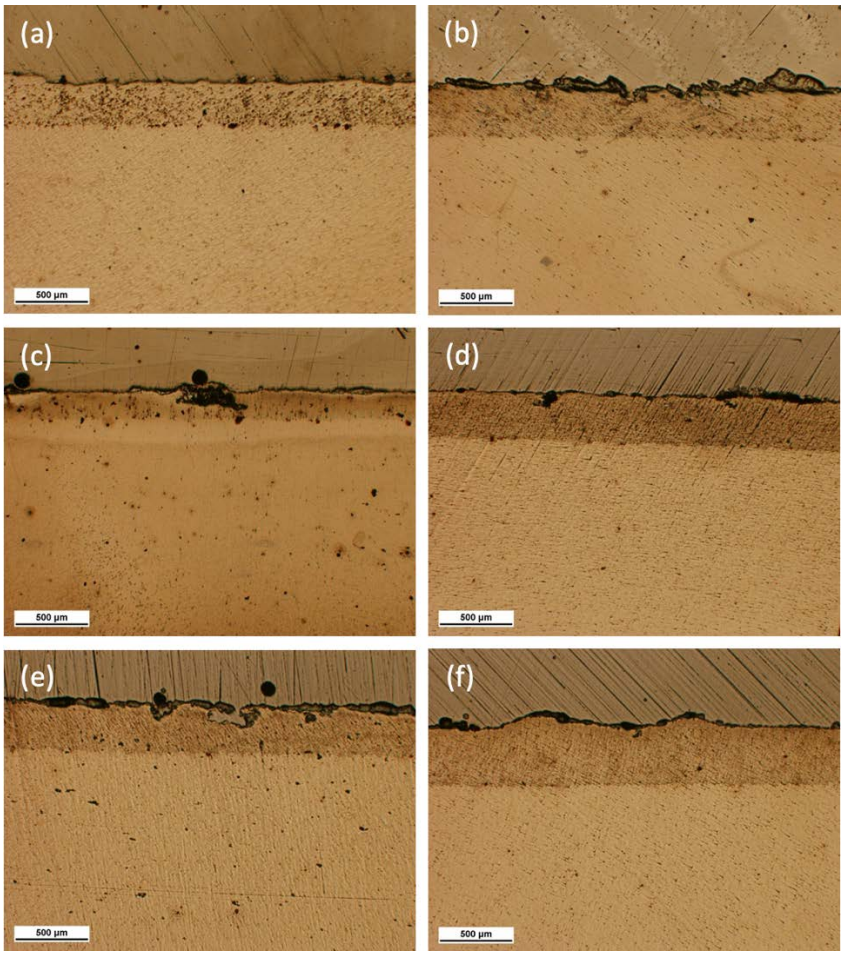


Figure 33. (a) Al, (b) Al-2vol% $nB_4C$, (c) Al-2vol% BNNP, (d) Al-1vol% $nB_4C$-1vol% BNNP, (e) Al-1vol% $nB_4C$-1vol% BNNP (3 mixings), and (f) Al-1.66vol% $nB_4C$-0.33vol% BNNP Coatings, Showing the Buildup of Aluminum Oxide and Relative Pitting Corrosion Between Each of the Coatings

Figure 33 demonstrates that coating 1 exhibits less corrosion than the other five coatings. Although the Figure 33 images are only one small area of each sample, they are representative of the coating behavior throughout the length of the sample. Coating 1 looks nearly pristine throughout the sample length while the other five coatings have pitting similar to the ones above. It appears that once there is an opening at the surface of the coating, the conditions inside the opening deteriorate and cause further corrosion. A higher magnification of a representative pit (from coating 3) using brightfield, darkfield, and SEM

imaging is depicted in Figure 34. Figure 34(c) appears flipped 180 degrees horizontally because of the reflection that occurs within the optical microscope.

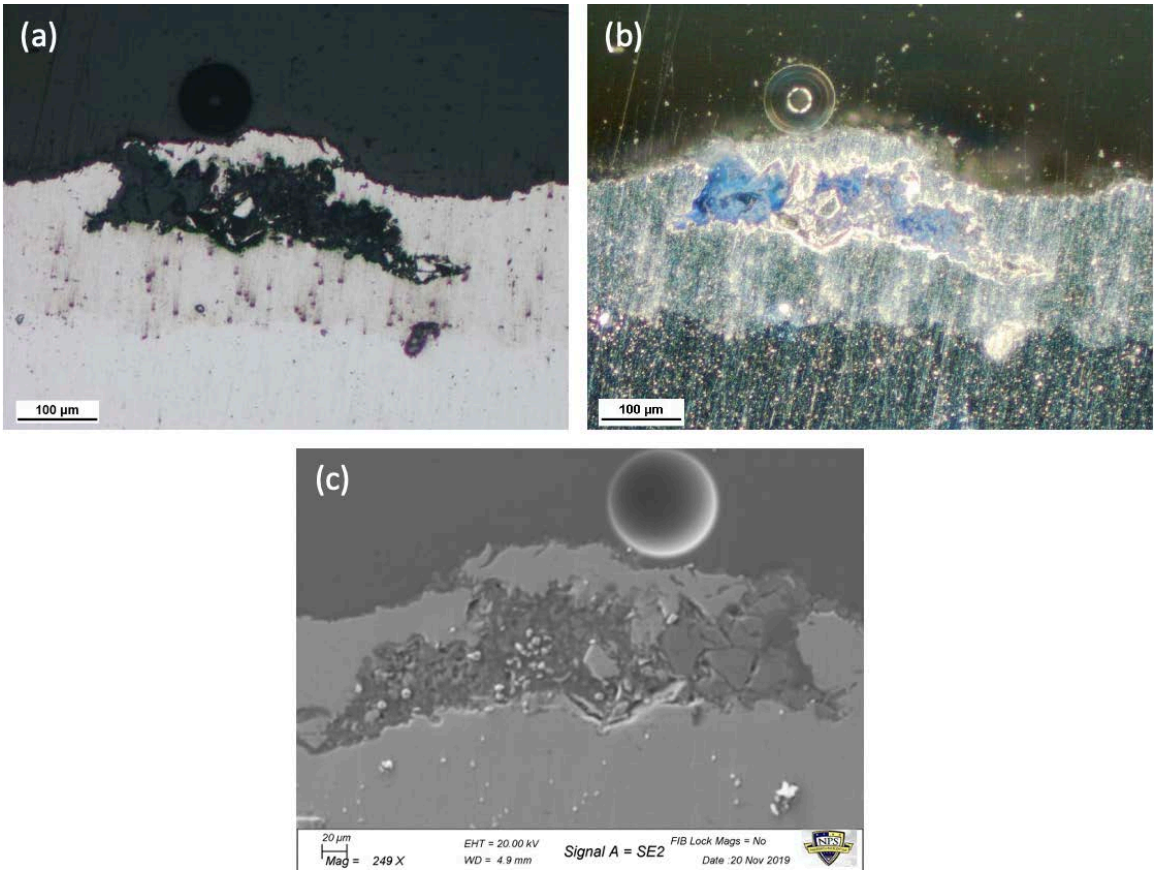


Figure 34. Coating 3 Higher Magnification of (a) Brightfield, (b) Darkfield, and (c) SEM Images of the Same Area as Shown in Figure 30(c).

In Figure 34, the corrosion has traversed over halfway through the entire coating after only 500 hours of salt fog chamber testing. It appears that corrosion starts on the left side of Figures 34(a) and 34(b) (right side of Figure 34(c)) and then undercuts through the uppermost part of the coating and leads to souring conditions within the pit. To understand what is occurring at the surface of the coating, it is important to consider the overall corrosion as having two different mechanisms—the initiation of corrosion and the propagation of corrosion through the coating.

The initiation of corrosion may result from a form of micro-crevice corrosion. In crevice corrosion, most of the system is oxygen rich. Oxygen is reduced in the bulk electrolyte from interaction with water and is subsequently replaced by more oxygen. However, under a crevice of any shape or size the amount of oxygen lowers because it cannot be replenished by more outside oxygen. This creates a concentration gradient between the bulk solution and the area under the crevice and results in the flow of current between the areas, oxidizing the metal under the crevice. Because the crevices in this case are so small, the anodic area experiences a high relative current density and can form quickly.

While none of the coatings display traditional crevice geometry like a gap underneath a bolt or screw, having a high roughness may be enough to create areas of low flow around a sharp asperity. This would prevent the replenishment of oxygen as described previously and result in the formation of a pit. One study looked at the effect of nanoparticles on the tribological behavior of alumina-based ceramic nanocomposite and found that a higher concentration of nanoparticles increased the surface roughness of the composite significantly. These results are depicted in Figure 35, where Ra refers to the average roughness of the surface and Rp refers to the maximum profile peak height. The nanoparticle used in the study was graphene nanoplatelets (GNP), which have a similar structure to BNNP [27].

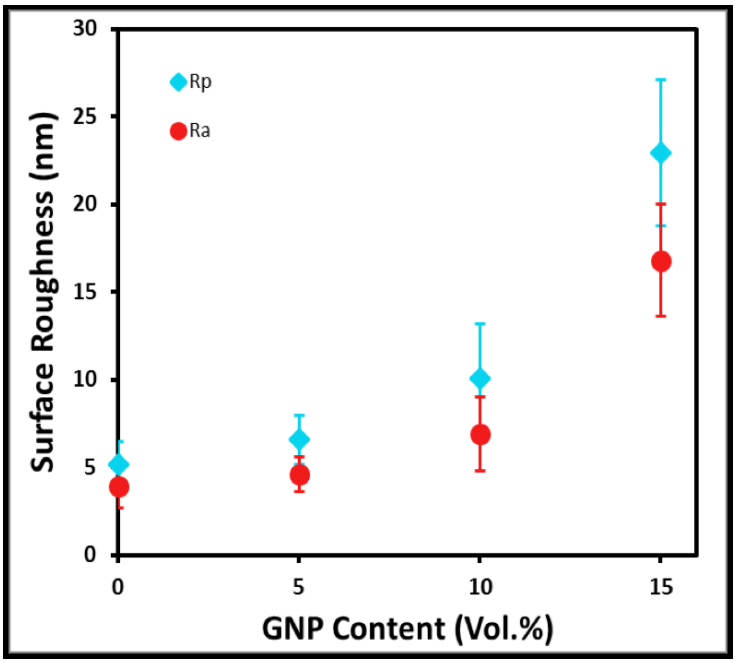


Figure 35. Effect of Graphene Nanoplatelet Concentration on the Surface Roughness of Aluminum Composites. Source: [27].

Extending the findings of the study shown in Figure 35, coatings 2 through 6 in the present research all contain 2 vol% nanoparticles. Coatings 3 through 6 contain BNNP. This is significant because the shape of the BNNP makes it likely that some of the particles extend slightly beyond the surface of the coating, creating a higher roughness and forming the micro crevice that could start the corrosion process. All of the coatings containing nanoparticles exhibit increased corrosion. However coating 3, which contains the largest amount of BNNP, yields the largest pit of all the coatings. This demonstrates the potential impact the micro crevice surface formations have on corrosion development.

Once the oxidation of the surface of the metal begins and a larger pit begins to form, the oxygen concentration reduces further, creating a larger electrical potential between the pit and the bulk material. Additionally, positively charged aluminum ions in the pit attract negatively charged chloride ions present in the environment into the pit, souring the conditions and accelerating the corrosion. This local environmental souring explains how the pit shown in Figure 34 is able to traverse over half of the cold sprayed coating. One

proposed mechanism of the corrosion of aluminum in a chloride environment is as follows at the anode [28]:

$$Al(s) \leftrightarrow Al^{3+}(aq) + 3e^{-}$$

$$Al^{3+}(aq) + 4Cl_4^{-}(aq) \leftrightarrow AlCl_4^{-}(aq)$$

and at the cathode [28]:

$$\frac{1}{2}O_2 + H_2O + e^{-} \leftrightarrow OH_{ads} + OH^{-}$$

When compared to the other samples, coating 1 does not contain ceramic nanoparticles within the coating feedstock. This lack of ceramic nanoparticles results in a surface condition lacking the micro crevices that enable the initiation of corrosion in the other five samples. Without these micro crevices, an initial pit is not formed that sours the environmental conditions and enhances localized corrosion. Therefore, coating 1 never develops the extensive pits seen in coatings 2 through 6. Additionally, the Introduction studies that demonstrated improved corrosion characteristics from cold spray coatings did not use ceramic nanoparticles [5] [7] and therefore would not have formed these micro crevices.

Characterizing each of the coatings, it is difficult to predict exactly which direction the pitting corrosion would progress. Figure 36 is an SEM image of Coating 2 etched following 500 hours of salt fog chamber testing and shows the path pitting corrosion takes through the top of the coating. The pitting corrosion results in a relatively large opening near the top of the coating that branches off into a series of smaller corrosion paths. Each of these corrosion paths are concave up in shape, matching the etched splat boundary shapes. It is possible the pitting corrosion progresses specifically along these splat boundaries because of the higher available free energy along these lines. This would indicate that using smaller sized aluminum particles as the base powder vice the ones used in this study would increase the number of splats in a cold sprayed coating. Using the same logic, this would increase the number of grain boundaries and small branches of corrosion.

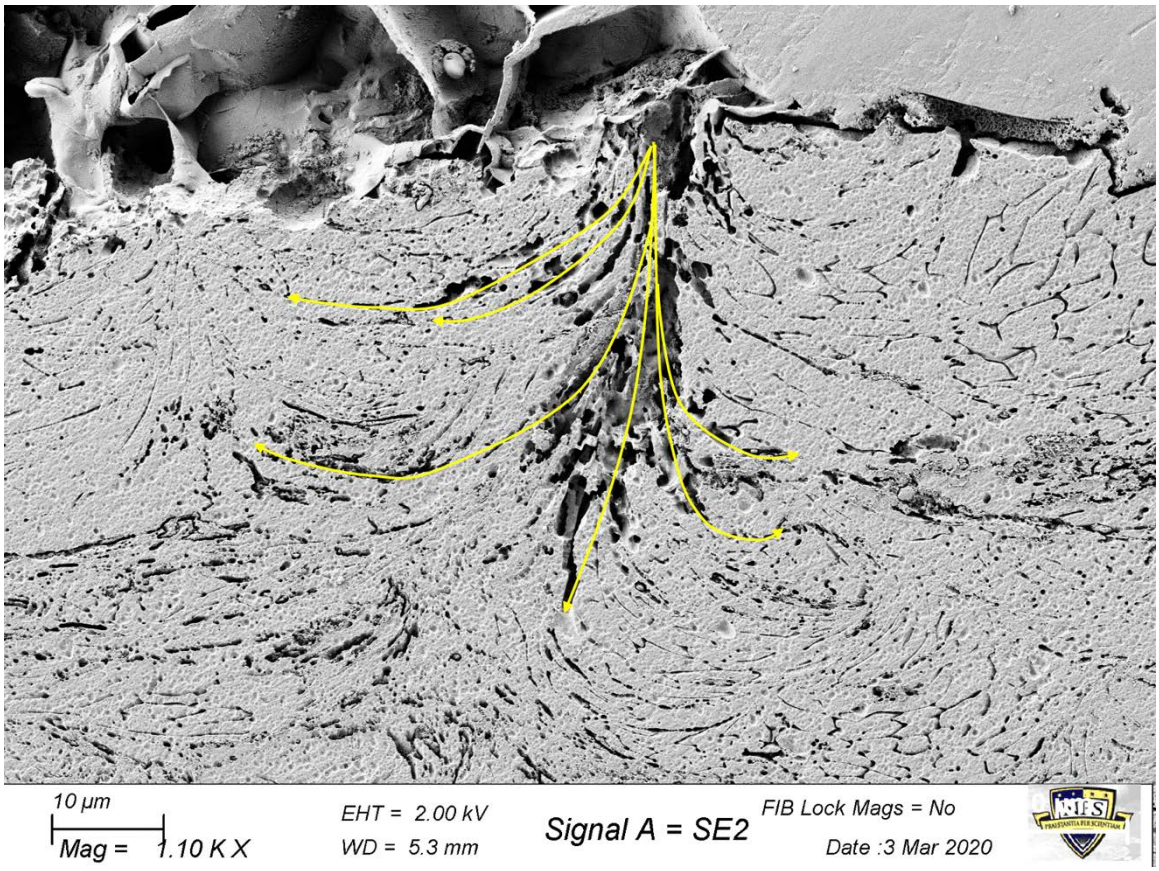


Figure 36. Etched Coating 2 Following 500 Hours of Corrosion Testing Showing Concave Up Paths of Corrosion As Indicated By Yellow Curves

### *b. Characterization of Oxide Layer*

Aluminum has a natural tendency to form a protective oxide layer, making it very corrosion resistant and preferable to use throughout the engineering industry. In a corrosive environment, aluminum will tend to corrode slightly, forming a thin oxide layer on the surface that acts as a boundary for diffusion of metal ions and arrests further corrosion. Following the 500-hour salt fog corrosion test, coating 6 was analyzed using EDS to determine the elemental composition in the vicinity of a pit. The results are depicted in Figure 37.

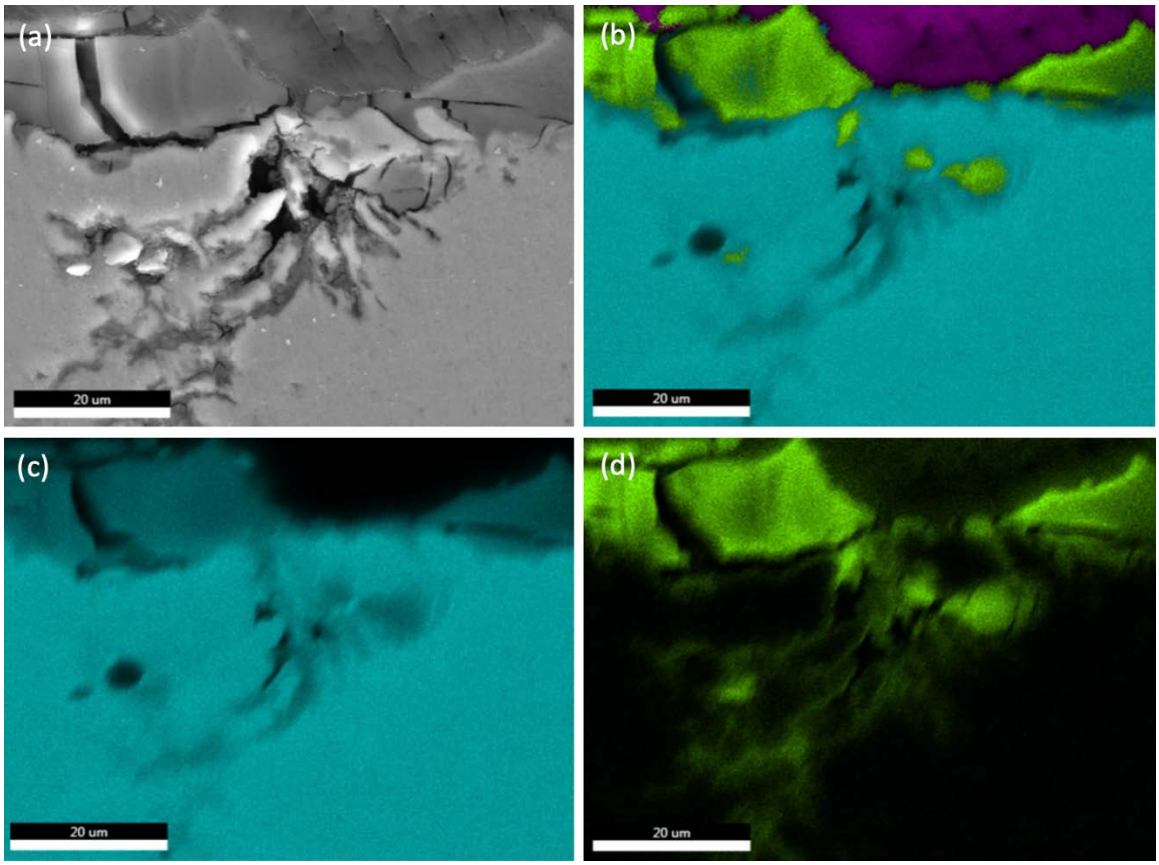


Figure 37. (a) SEM Image, (b) All EDS Elemental Overlay, (c) Only Aluminum, and (d) Only Oxygen, Showing a Lack of Aluminum Oxide Over the Entrance to the Pit in the Coating.

Figure 37 shows a pit that has formed on coating 6 similar to the pit on coating 2 depicted in Figure 36. Figure 37(a) is the base SEM image with no elemental overlays. It appears that there is an oxide layer in Figure 37(a) that is approximately 15–20 microns in thickness. In Figure 37(a), there is a clear entrance to the pit in the coating that corresponds to a lack of oxygen depicted in Figure 37(d). If there were a continuous oxide coating through the entire surface, it is unlikely that the severe pitting would have occurred. It is not clear whether the passive oxide layer formed and subsequently deteriorated, allowing the corrosion to occur, or if the presence of the micro crevices due to the ceramic nanoparticles interfered with the formation of a cohesive protective oxide layer.

The image in Figure 37(a) also closely matches the “corrosion tunneling” observed by Xie et al. [29]. In this study, the author observed a tortuous path of corrosion tunneling

into a cold sprayed zinc coating during an immersion test with 3.5 wt% NaCl - the same NaCl concentration as this research. The presence of multiple tortuous paths in the study was a result of extensive plastic deformation resulting from the cold spray process. Tunneling through the coating allowed the electrolyte (NaCl) to penetrate farther into the coating and aided in the pitting corrosion already discussed. Greater porosity would also be more conducive to a facile corrosion path thru splat boundaries, due to electrolyte infiltration.

An XRD analysis was performed in addition to the EDS analysis in order to verify the presence of aluminum oxide from a crystal structure standpoint vice a spectroscopy standpoint. The results of the test are shown in Figure 38 for coatings 1 and 4.

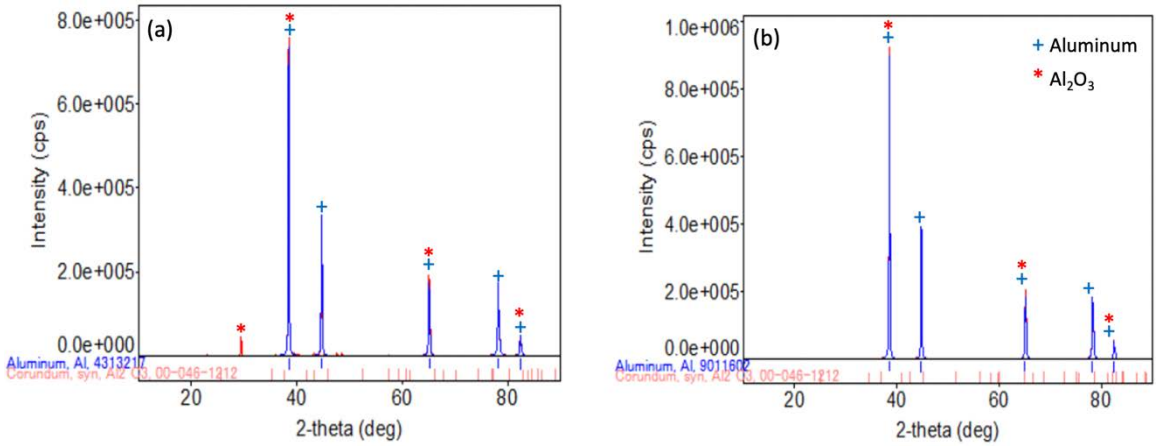


Figure 38. XRD Results for (a) Coating 1 and (b) Coating 4 Showing Peaks for Aluminum and Aluminum Oxide

The only peaks identified in the analysis are for Al and $Al_2O_3$. The aluminum oxide comprises 8.81 and 7.95 wt % of the surface for coatings 1 and 4 respectively. Aluminum makes up most of the coating, so it is not surprising that was represented. Neither of the ceramic reinforcements show up in the test because they only compose 2 vol% of the total volume in coating 4.

Using the SEM to look at the top surface of coating 1 yields the results in Figure 39. Initially it appears that there are two types of morphology on the surface of the corroded

cold spray coating - a soft, porous looking structure and a hard, brittle structure with extensive cracking. Upon further inspection, the hard, brittle structure is determined to be aluminum oxide because it matches the characteristics of the aluminum oxide observed in the cross-sectioned samples. In both the top view of Figure 39 and the cross-section views of Figures 34 and 37, the structure on top of the cold sprayed coating is non-uniform and exhibits extensive cracking throughout. An EDS analysis of the top of Coating 2 was performed and provided the results of Figure 40, confirming that the soft, porous structure is not a different phase of aluminum oxide. Instead, it is NaCl deposited on the surface of the aluminum oxide. This deposition is expected to occur in the salt fog chamber, where the dense mist generated was 3.5% NaCl. Furthermore, sodium and chlorine are present in equal amounts in the EDS results, making NaCl the stoichiometrically preferred compound. On the right side of the images in Figure 40(b) and 40(c), there are very little x-ray returns because of the vertically-oriented aluminum oxide face observed in Figure 40(a). This location is in a small valley on the surface of the sample, making it unlikely that x-rays emitted from the deeper areas would reach the detector and be represented in the report. This is because as x-rays are emitted from atoms within the valley of the surface in Figure 40(a), they will be absorbed by other atoms prior to reaching the detector. In this case, the elements within the valley are underrepresented. It is possible that NaCl deposited on the surface of the aluminum oxide would have a detrimental effect on the cold sprayed coating underneath because it could get in between the cracks of the oxide and cause further corrosion of the coating.

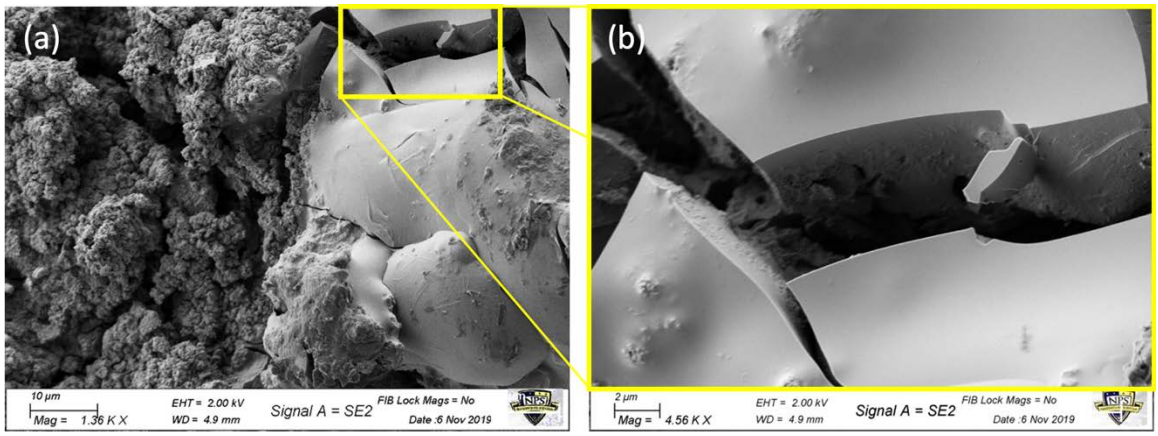


Figure 39. SEM Image of Coating 1 Oxide Layer on Top Surface

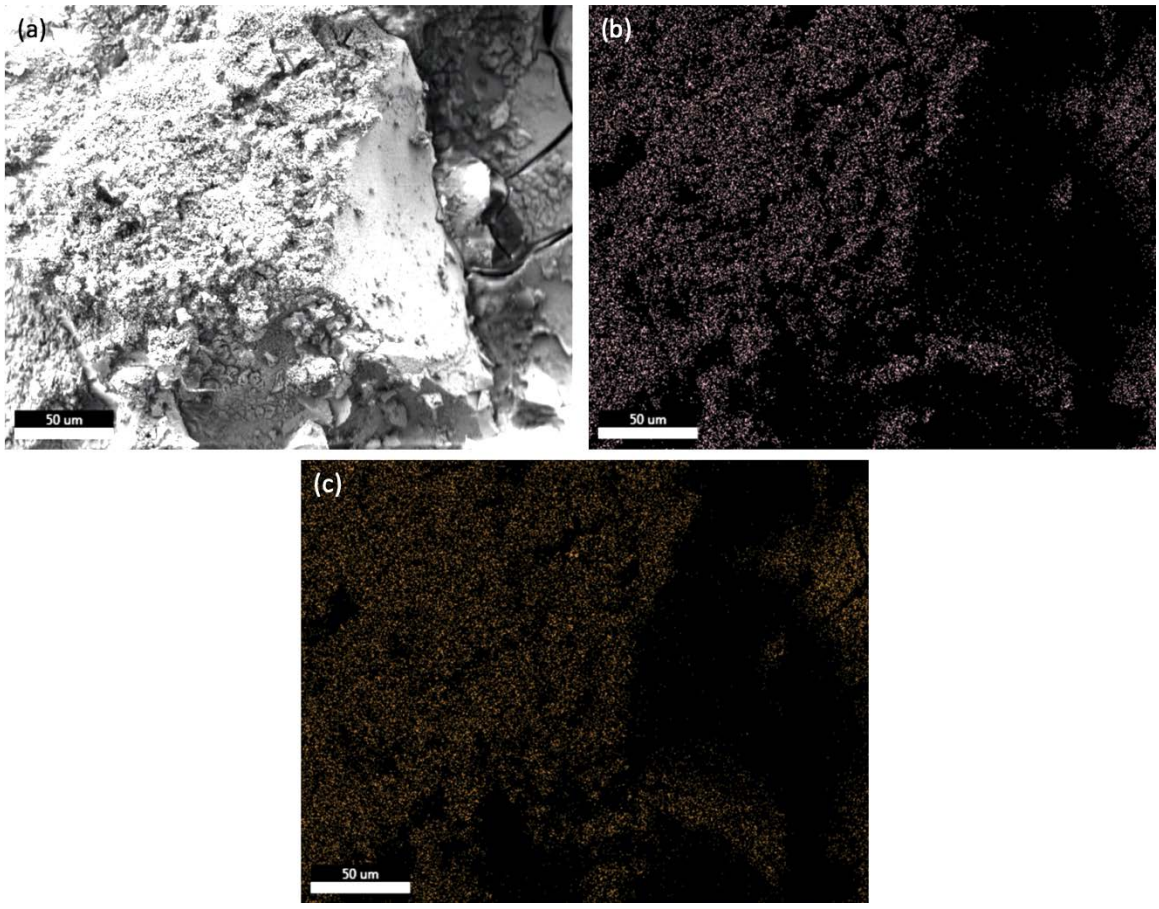


Figure 40. Coating 2 Top View of an (a) SEM Image and (b) EDS Overlay of Sodium and (c) Chlorine Elements

### 2. 2000-Hour Samples

#### *a. Visual/SEM Characterization*

The 2000-hour corrosion test samples exhibit similar visual characteristics to the 500-hour corrosion test samples, except that the salt residue on the surface of the samples is more pronounced. Coatings 2 and 6, consisting of the highest vol% $nB_4C$, have the thickest appearing deposits as shown in Figure 41. This is consistent with Table 7 showing the mass and thickness gains over time for the samples. Coatings 2 and 6 exhibit a significantly higher mass gain and thickness gain over the span of the corrosion test. This matches the results of the 500-hour corrosion test that was performed on different samples, indicating repeatability of the test and a consistent underlying mechanism of corrosion.

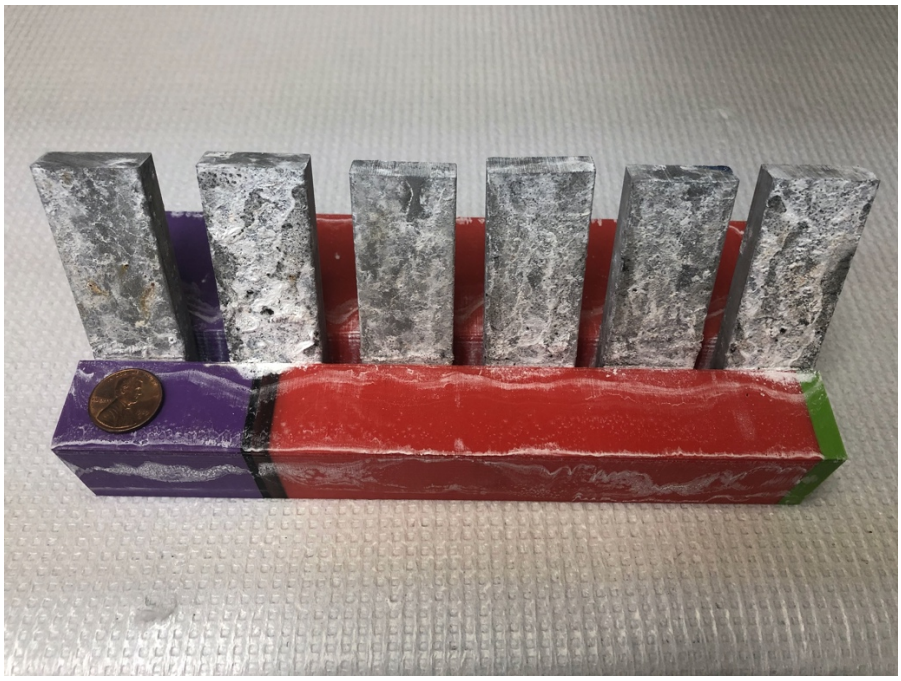

Figure 41. Sample Coatings in Order 1 Through 6, from Left to Right, Following 2000 Hours in a Salt Fog Chamber Accelerated Corrosion Test

Coating 1 has the lowest mass gain out of all the samples, indicating that there is less corrosion than every other sample and that adding ceramic nanoparticles consistently results in more corrosion of the coating. Figure 42 shows brightfield optical microscope

images of the six coatings following 2000-hours in the salt fog chamber. For the 2,000-hour samples, two cross sections were examined by grinding down the back side of the puck. While coating 1 appears nearly pristine across the entire length of the cross section observed in the 500-hour test, there is a single pit in the 2000-hour cross sections. Per the mechanism of corrosion proposed in the 500-hour test, there should have been minimal pitting in the control sample in a longer duration corrosion test because there are no nanoparticles within the coating. In the pit observed in Figure 42(a), the cold spray application may have created a natural roughness that led to a crevice and the onset of corrosion. This natural crevice without nanoparticles would not be very likely to occur because of the elongated splats that occur in cold spray, explaining why there is only one pit observed over the length of two cross sections for coating 1.

Table 7. (a) Mass and (b) Thickness Measurements for 2,000-hour Samples

| (a) | 0 hours (initial) | 2,012 hours (final) | Change from initial |
|---|---|---|---|
| Sample | Mass (g) | | |
| 1B | 43.88 | 43.97 | +0.09 |
| 2B | 44.75 | 45.25 | +0.50 |
| 3B | 42.98 | 43.11 | +0.13 |
| 4B | 44.68 | 44.86 | +0.18 |
| 5B | 44.24 | 44.4 | +0.16 |
| 6B | 44.25 | 44.61 | +0.36 |

| (b) | 0 hours (initial) | 2,012 hours (final) | Change from initial |
|---|---|---|---|
| Sample | Thickness (mm) | | |
| 1B | 9.70 | 10.01 | +0.31 |
| 2B | 9.70 | 10.56 | +0.86 |
| 3B | 9.80 | 9.97 | +0.17 |
| 4B | 9.70 | 10.11 | +0.41 |
| 5B | 9.90 | 10.20 | +0.30 |
| 6B | 9.70 | 10.28 | +0.58 |

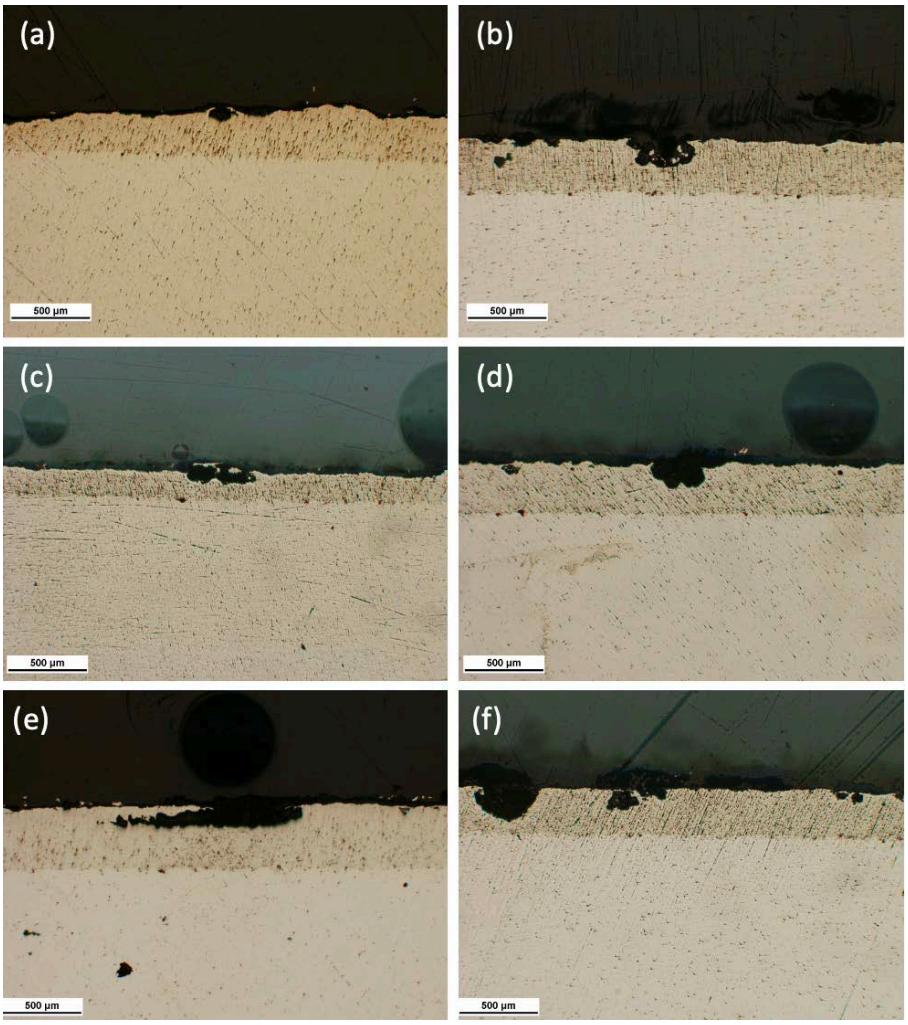


Figure 42. (a) Al, (b) Al-2vol% $nB_4C$, (c) Al-2vol% BNNP, (d) Al-1vol% $nB_4C$-1vol% BNNP, (e) Al-1vol% $nB_4C$-1vol% BNNP (3 mixings), and (f) Al-1.66vol% $nB_4C$-0.33vol% BNNP Coatings Showing the General Corrosion of 2000-hour Samples

A primary distinction between the 500-hour and 2000-hour corrosion tests is extensive corrosion along the interface of the coatings and substrates in most of the samples observed for the 2000-hour test. In Figure 43, there is significant corrosion eating away at both the metal and the substrate. This is very likely initiated by galvanic corrosion at the interface. Galvanic corrosion likely initiates micro-crevices at the coating/substrate interface, that then become active pitting sites. After initiation, corrosion becomes severe due to simultaneous pitting and galvanic corrosion at the interface. In this case the galvanic corrosion does not have subside following initiation of current flow and loss of metal.

Instead, the galvanic corrosion continues in addition to pitting corrosion. Coatings 3 and 6, depicted in Figure 43(c) and 43(f) respectively, can be considered a more advanced stage of corrosion depicted in coating 2, depicted in Figure 43(b). In coatings 3 and 6, the pit formed on top of the coating traverses through the coating down to the area initiated by galvanic corrosion and causes a portion of the coating to detach completely. At this point, the area previously covered by the coating is completely exposed to the corrosive environment.

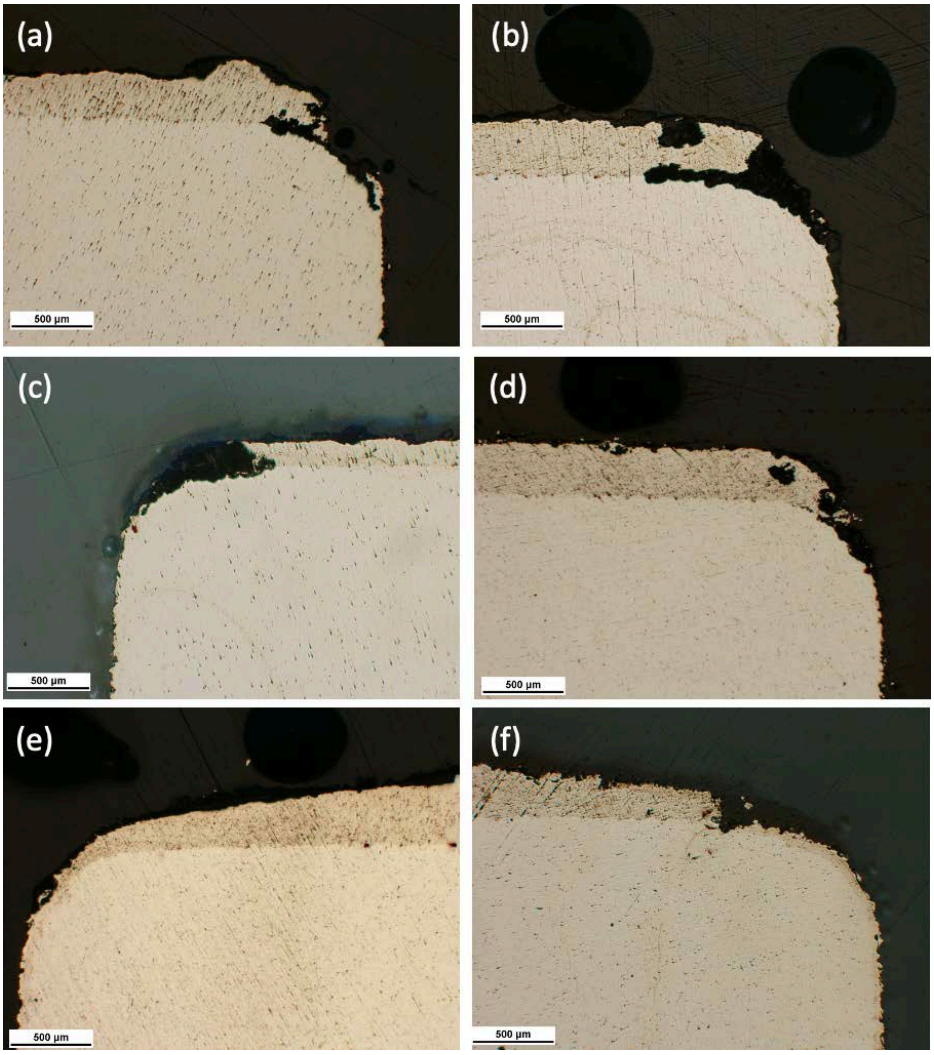


Figure 43. Edge of (a) Al, (b) Al-2vol% $nB_4C$, (c) Al-2vol% BNNP, (d) Al-1vol% $nB_4C$-1vol% BNNP, (e) Al-1vol% $nB_4C$-1vol% BNNP (3 mixings), and (f) Al-1.66vol% $nB_4C$-0.33vol% BNNP Coatings Showing Galvanic Corrosion at Coating Interface

Not only does galvanic corrosion initiate at the interface of the coating and degrade the coating, but it also initiates corrosion of the substrate as shown in Figure 44 - an SEM image of the same area captured in coating 2, Figure 43(b). Again, the optical and SEM images are flipped 180 degrees horizontally because of the reflection occurring within the optical microscope. Figure 44 shows corrosion of the AA6061 substrate 736 µm down from the interface of the coating and substrate. Closer to the interface, there is a higher degree of corrosion of the substrate. Below 736 µm away from the interface as indicated on the image, there is minimal corrosion of the substrate. This indicates that the corrosion of the substrate is correlated to its proximity to the interface and is a consequence of galvanic corrosion.

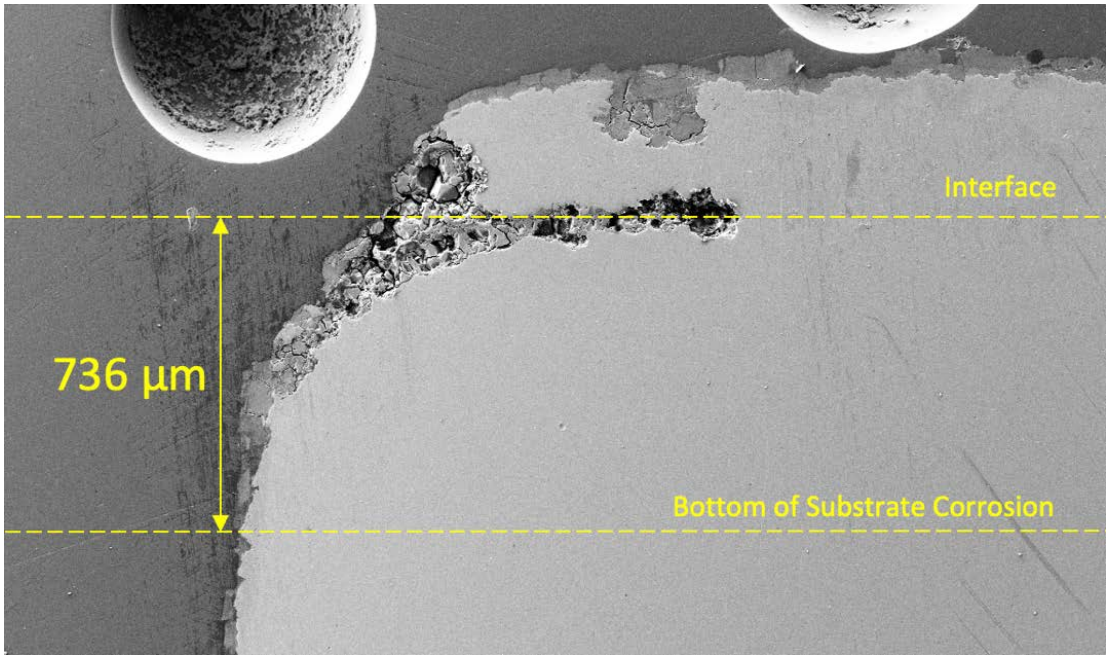


Figure 44. Substrate Corrosion of Coating 2 Following 2000 Hours in Salt Fog Chamber

Figure 45 shows the corrosion of coating 2 at increasing magnifications, focusing on the galvanic corrosion at the interface of the coating and substrate. Throughout the area corroded in Figure 45(a), there is extensive cracking of aluminum oxide as observed in other corroded samples. In Figure 45(b), corrosion is oxidizing the metal coating and metal

substrate in approximately equal amounts above and below the interface. As the galvanic corrosion progresses through the interface, it does not migrate either above or below the interface line - instead it proceeds along the interface line where there is the electric potential difference between the coating and substrate. Figure 45(c) is a high magnification image of the leading tip of the corrosion focusing at the interface, showing where the metal starts to oxidize prior to removal from the salt fog chamber. The corroded area in this figure is only a fraction of the area exposed earlier in the test, but already there is the same cracking of aluminum oxide evident in nearly every other area of corrosion. This indicates that aluminum oxide was formed immediately around the sites of aluminum corrosion but that it is not necessarily protective because of the presence of chlorides in an aerated environment, as noted by Xhanari and Finsgar [30].

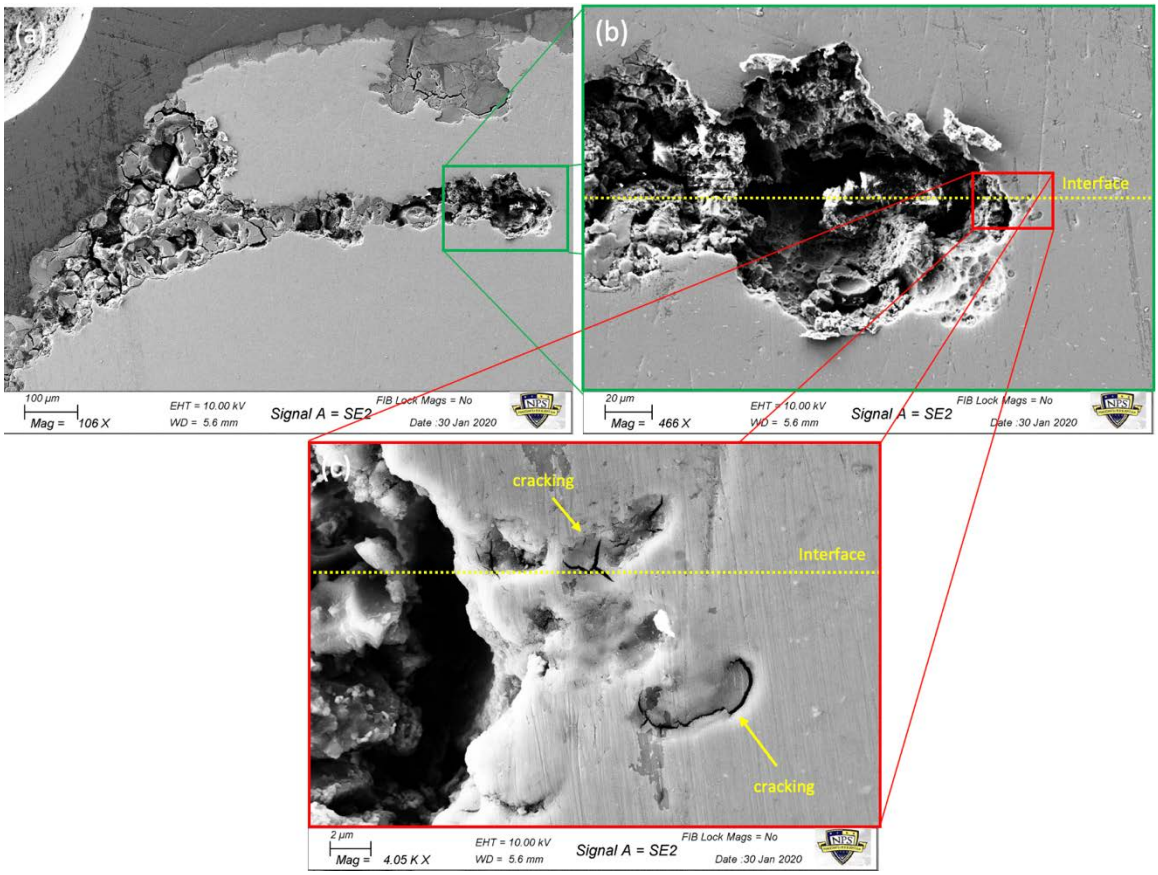


Figure 45. Coating 2 Cross Section Showing Galvanic and Pitting Corrosion at (a) Low Mag, (b) Intermediate Mag, and (c) High Mag

If the corrosion were limited to the coating or even a thin penetration of the substrate, the cold sprayed coatings could be used in limited applications where they would be exposed to a marine (chloride) environment. Instead, the substrate is corroded because of the coatings that were applied. Figure 46 shows how corrosion continues into the substrate after the galvanic corrosion passes over the location in Figure 46(b). As mentioned previously, in the bottom of Figure 44 a “large” distance away from the cold sprayed, there is hardly any corrosion of the substrate. In this scenario it can be argued that the cold sprayed coatings actually have a negative impact on the substrate they are intended to protect from an austere environment.

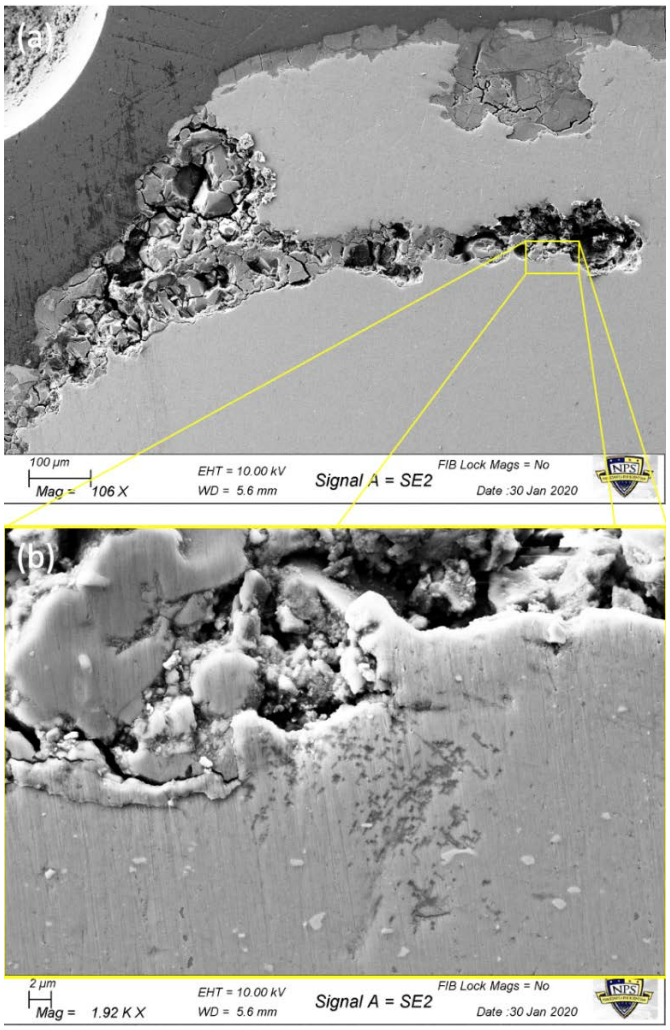


Figure 46. Coating 2 Cross Section Showing Galvanic and Pitting Corrosion into the (a) Coating and (b) Substrate

# IV. CONCLUSIONS

This study elucidates the benefits and challenges with using ceramic nanoparticles to reinforce an aluminum matrix when used in a high-pressure cold spray application. It is meant to provide a compass rose for future studies to take the best performing coatings and further refine them to produce an even stronger, harder matrix that could be used to repair components in engineering applications across the industry and Department of Defense. To that end, the Al-1vol% n$B_4C$-1vol% BNNP (single step cryomill) coating achieves the highest increase in hardness using a relatively low volume percent ceramic reinforcement consisting of a 1:1 ratio of BNNP and n$B_4C$ within the aluminum matrix. Al-1vol% nB4C-1vol% BNNP also minimizes the variation in hardness values amongst the composite coatings, indicating that cryomilling is essential for the final powder processing prior to cold spray. The 1:1 ratio of the two reinforcement nanoparticles requires further investigation to determine the optimum total reinforcement within the composite matrix.

Additionally, the cold spray application was performed using state-of-the-art equipment, with carrier gas pressures over the normally considered limit for “high pressure” cold spray. This is intended as a proof-of-concept for dual nanoparticle reinforcements and could be used widespread within the engineering field, but relatively few facilities have such capability. This high-pressure cold spray could also be used for repair in niche high performance applications such as high-speed brakes or pump bearings.

Wear testing of each coating was performed, but most of the tests drove through the coatings into the substrate, indicating more refinement of the testing parameters is required. The corrosion studies performed in this research produced less than ideal results. Specifically, the coatings containing the highest amounts of n$B_4C$ consistently yield the highest thickness and mass gains over both 500- and 2000-hour trials, indicating that it is not a useful reinforcement from a corrosion standpoint. Additionally, these coatings exhibit severe pitting and galvanic corrosion, rendering them ineffective in protecting the substrate underneath. The corrosion occurs within a marine

environment, indicating that using these coatings topside onboard U.S. Navy ships would not be a long-term solution to repairing a crack or other structural deficiency. Instead, they would be more useful within interior spaces that have much more limited exposure to the harsh marine environment at sea.

# V. RECOMMENDATIONS FOR FUTURE STUDY

- Considering the five composite coatings contain relatively low volume percent reinforcements, higher reinforcement percentages should be explored, ranging from 5 to 50 vol%.
- Applying similar coatings using a low-pressure application would determine if the positive results observed in hardness testing are a function of the high pressure used or if similar results could be obtained in more mobile facilities.
- Using a portable cold spray unit with a handheld gun to apply coatings similar to the ones in this study would prove the viability of this technology onboard U.S. Navy ships to repair metal bearings, stanchions, or other in-situ structures. This would enable ship's company to increase the readiness condition of their ship nearly immediately following the discovery of a metal crack or failure and would ultimately save money from expensive repairs needing to occur in shipyard availabilities.
- In order to further validate these results and rule out using $nB_4C$ completely in a marine environment, cold sprayed coatings similar to the ones used in this study should be subjected to an immersion test vice a salt fog chamber test. In an immersion test, the electrolyte could be made identical in composition to the electrolyte in the 3.5% NaCl salt fog chamber test but would have a significantly higher density. This would increase the rate of corrosion and would serve as another data point to confirm the negative impact of $nB_4C$ on cold sprayed coatings in an austere environment.
- Larger sized powder reinforcements could be added vice nano-scale reinforcements to test theory of nanoparticles driving a higher roughness that provides sites for pitting corrosion to commence.
- Using the same substrate alloy, in this case AA6061, for the base powder in a cold sprayed coating should greatly reduce the amount of galvanic corrosion that occurred at the interface between the coating and substrate.

- Heat treatment of the cold sprayed coatings would help determine if changes in porosity can further increase the hardness and corrosion resistance of the composite coating.

# APPENDIX A. COMPLETE HARDNESS DATA

All hardness values are in HV.

| | Point | | | | | | | | | | | | |
|---|---|---|---|---|---|---|---|---|---|---|---|---|---|
| Coating | 1 | 2 | 3 | 4 | 5 | 6 | 7 | 8 | 9 | 10 | Average | Standard Deviation | Percent Change |
| 1 | 58.6 | 57.1 | 58.4 | 57.3 | 53.6 | 56.6 | 55.5 | 55.8 | 58.4 | 61.8 | 57.3 | 2.21 | 0.00 |
| 2 | 57.0 | 63.0 | 60.2 | 50.0 | 54.5 | 55.3 | 61.8 | 53.4 | 60.3 | 57.6 | 57.3 | 4.09 | 0.00 |
| 3 | 59.8 | 58.4 | 61.3 | 64.5 | 62.7 | 57.1 | 63.0 | 58.7 | 62.7 | 64.8 | 61.3 | 2.67 | +6.96 |
| 4 | 61.8 | 64.8 | 59.2 | 67.4 | 63.9 | 62.4 | 67.4 | 63.9 | 63.9 | 64.8 | 64.0 | 2.47 | +11.59 |
| 5 | 65.1 | 49.8 | 60.9 | 62.4 | 64.5 | 64.5 | 63.9 | 64.8 | 66.4 | 65.8 | 62.8 | 4.84 | +9.60 |
| 6 | 60.9 | 60.1 | 63.3 | 65.1 | 59.2 | 64.2 | 60.9 | 67.4 | 58.7 | 63.3 | 62.3 | 2.80 | +8.72 |

THIS PAGE INTENTIONALLY LEFT BLANK

# APPENDIX B. MASS AND THICKNESS MEASUREMENTS FOR CORROSION SAMPLES

Notation of “A” refers to 500-hr corrosion test and notation of “B” refers to 2000-hr corrosion test.

| | Mass (g) Of Samples vs. Time in Salt Fog Chamber | | | | | | | | | | | | |
|---|---|---|---|---|---|---|---|---|---|---|---|---|---|
| Time (h) | 0 | 168 | 336 | 504 | 672 | 840 | 1,008 | 1,176 | 1,344 | 1,512 | 1,680 | 2,016 | Change From Initial |
| 1A | 44.33 | 44.37 | 44.47 | 44.43 | | | | | | | | | +0.10 |
| 2A | 43.91 | 44.15 | 44.23 | 44.26 | | | | | | | | | +0.35 |
| 3A | 42.98 | 43.02 | 43.11 | 43.1 | | | | | | | | | +0.12 |
| 4A | 44.6 | 44.74 | 44.79 | 44.72 | | | | | | | | | +0.12 |
| 5A | 44.16 | 44.32 | 44.32 | 44.25 | | | | | | | | | +0.09 |
| 6A | 43.96 | 44.2 | 44.22 | 44.18 | | | | | | | | | +0.22 |
| 1B | 43.88 | 43.9 | 43.99 | 43.94 | 43.93 | 43.9 | 43.96 | 43.94 | 43.97 | 43.94 | 43.96 | 43.97 | +0.09 |
| 2B | 44.75 | 45.07 | 45.07 | 45.05 | 45.08 | 45.04 | 45.15 | 45.18 | 45.15 | 45.16 | 45.2 | 45.25 | +0.50 |
| 3B | 42.98 | 43.05 | 43.13 | 43.09 | 43.06 | 43.07 | 43.11 | 43.15 | 43.11 | 43.1 | 43.1 | 43.11 | +0.13 |
| 4B | 44.68 | 44.83 | 44.85 | 44.87 | 44.8 | 44.78 | 44.84 | 44.84 | 44.84 | 44.87 | 44.82 | 44.86 | +0.18 |
| 5B | 44.24 | 44.38 | 44.42 | 44.37 | 44.34 | 44.35 | 44.36 | 44.39 | 44.38 | 44.42 | 44.38 | 44.4 | +0.16 |
| 6B | 44.25 | 44.49 | 44.54 | 44.45 | 44.49 | 44.46 | 44.51 | 44.57 | 44.54 | 44.57 | 44.56 | 44.61 | +0.36 |

| | Thickness (mm) of Samples vs. Time in Salt Fog Chamber | | | | | | | | | | | | |
|---|---|---|---|---|---|---|---|---|---|---|---|---|---|
| Time (h) | 0 | 168 | 336 | 504 | 672 | 840 | 1,008 | 1,176 | 1,344 | 1,512 | 1,680 | 2,016 | Change From Initial |
| 1A | 9.70 | 9.80 | 9.92 | 9.80 | | | | | | | | | +0.10 |
| 2A | 9.70 | 10.00 | 10.10 | 10.10 | | | | | | | | | +0.40 |
| 3A | 9.70 | 9.70 | 9.78 | 9.80 | | | | | | | | | +0.10 |
| 4A | 9.70 | 9.90 | 9.93 | 9.90 | | | | | | | | | +0.20 |
| 5A | 9.90 | 9.90 | 10.10 | 10.00 | | | | | | | | | +0.10 |
| 6A | 9.70 | 9.90 | 10.06 | 9.90 | | | | | | | | | +0.20 |
| 1B | 9.70 | 9.80 | 9.90 | 9.80 | 9.80 | 9.92 | 9.90 | 9.88 | 9.90 | 9.95 | 9.97 | 10.01 | +0.31 |
| 2B | 9.70 | 9.90 | 10.10 | 9.90 | 10.10 | 10.20 | 10.3 | 10.40 | 10.28 | 10.38 | 10.50 | 10.56 | +0.86 |
| 3B | 9.80 | 9.70 | 9.80 | 9.70 | 9.80 | 9.80 | 9.92 | 9.85 | 9.80 | 9.94 | 9.92 | 9.97 | +0.17 |
| 4B | 9.70 | 9.80 | 9.95 | 9.90 | 10.00 | 10.09 | 10.25 | 9.98 | 9.95 | 10.03 | 10.12 | 10.11 | +0.41 |
| 5B | 9.90 | 9.90 | 10.10 | 9.90 | 10.00 | 10.08 | 10.09 | 10.13 | 10.01 | 10.08 | 10.16 | 10.20 | +0.30 |
| 6B | 9.70 | 9.90 | 10.10 | 10.00 | 10.10 | 10.20 | 10.16 | 10.20 | 10.13 | 10.25 | 10.26 | 10.28 | +0.58 |

# LIST OF REFERENCES


[1] S. Kuroda, J. Kawakita, M. Watanabe and H. Katanoda, “Warm spraying—a novel coating process based on high-velocity impact of solid particles,” *Science and Technology of Advanced Materials,* vol. 9, Jul. 2008. [Online]. 10.1088/1468-6996/9/3/033002

[2] J. Matejicek, R. Musalek and J. Veverka, “Materials and processing factors influencing stress evolution and mechanical properties of plasma sprayed coatings,” *Surface Coatings and Technology*, vol. 371, pp. 3–13, Aug. 2019. [Online]. https://doi.org/10.1016/j.surfcoat.2019.01.105

[3] G. Mauer, R. VaBen and D. Stover, “Plasma and particle temperature measurements in thermal spray: Approaches and applications,” *Journal of Thermal Spray Technology*, vol. 20, pp. 391–406, Mar. 2011. [Online]. https://doi.org/10.1007/s11666-010-9603-z

[4] C. A. Widener, O. C. Ozdemir and M. Carter, “Structural repair using cold spray technology for enhanced sustainability of high value assets,” *Procedia Manufacturing,* vol. 21, pp. 361–368, Mar. 2018. [Online]. https://doi.org/ 10.1016/j.promfg.2018.02.132

[5] S. Ngai, T. Ngai, F. Vogel, W. Story, G. B. Thompson and L. N. Brewer, “Saltwater corrosion behavior of cold sprayed AA7075 aluminum alloy coatings,” *Corrosion Science,* vol. 130, pp. 231–240, Jan. 2018. [Online]. https://doi.org/ 10.1016/j.corsci.2017.10.033

[6] E. McCafferty, *Introduction to Corrosion Science,* Alexandria, VA, USA: Springer, 2010.

[7] M. Diab, X. Pang and H. Jahed, “The effect of pure aluminum cold spray coating on corrosion and corrosion fatigue of magnesium (3% Al-1% Zn) extrusion,” *Surface Coatings and Technology,* vol. 309, pp. 423–435, Jan. 2017. [Online]. https://doi.org/10.1016/j.surfcoat.2016.11.014

[8] Y. T. R. Lee, H. Ashrafizadeh, G. Fisher and A. McDonald, “Effect of type of reinforcing particles on the deposition efficiency and wear resistance of low-pressure cold-sprayed metal matrix composite coatings,” *Surface and Coatings Technology*, vol. 324, pp. 190–200, Sep. 2017. [Online]. https://doi.org/10.1016/ j.surfcoat.2017.05.057

[9] R. Raoelison, Y. S. T. Xie, M. Planche, R. Kromer, S. Costil and C. Langlade, "Cold gas dynamic spray technology: A comprehensive review of processing conditions for various technological developments till to date," *Additive Manufacturing*, vol. 19, pp. 134–159, Jan. 2018. [Online]. https://doi.org/10.1016/j.addma.2017.07.001

[10] D. Gilmore, R. Dykhuizen, R. Neiser, T. Roemer and M. Smith, "Particle velocity and deposition efficiency in the cold spray process," *Journal of Thermal Spray Technology*, vol. 8, pp. 576–582, Dec. 1999. [Online]. https://doi.org/10.1361/105996399770350278

[11] M. Yandouzi, A. Bottger, R. Hendrikx, M. Brochu, P. Richer, A. Charest and B. Jodoin, "Microstructure and mechanical properties of $B_4C$ reinforced Al-based matrix composite coatings deposited by CGDS and PGDS processes," *Surface and Coatings Technology*, vol. 205, pp. 2234–2246, Dec. 2010. [Online]. https://doi.org/10.1016/j.surfcoat.2010.08.143

[12] F. Thevenot, "Boron carbide - A comprehensive review," *Journal of the European Ceramic Society*, vol. 6, pp. 205–225, Apr. 1990. [Online]. https://doi.org/10.1016/0955-2219(90)90048-K

[13] N. Tariq, L. Gyansah, J. Wang, X. Qiu, B. Feng, M. Siddique and T. Xiong, "Cold spray additive manufacturing: A viable strategy to fabricate thick $B_4C$/Al composite coatings for neutron shielding applications," *Surface and Coatings Technology*, vol. 339, pp. 224–236, Apr. 2018. [Online]. https://doi.org/10.1016/j.surfcoat.2018.02.007

[14] O. Ormanci, I. Akin, F. Sahin, O. Yucel, V. Simon, S. Cavalu and G. Goller, "Spark plasma sintered $Al_2O_3$–YSZ–$TiO_2$ composites: Processing, characterization and in vivo evaluation," *Materials Science and Engineering*, vol. 40, pp. 16–23, Jul. 2014. [Online]. https://doi.org/10.1016/j.msec.2014.03.041

[15] A. Nieto, H. Yang, L. Jiang and J. M. Schoenung, "Reinforcement size effects on the abrasive wear of boron carbide reinforced aluminum composites," *Wear*, Vols. 390–391, pp. 228–235, Nov. 2017. [Online]. https://doi.org/10.1016/j.wear.2017.08.002

[16] Y. Song, G. He, Y. Wang and Y. Chen, "Tribological behavior of boron nitride nanoplatelet reinforced $Ni_3Al$ intermetallic matrix composite fabricated by selective laser melting," *Materials and Design*, vol. 165, Mar. 2019. [Online]. https://doi.org/10.1016/j.matdes.2018.107579

[17] B. Lee, D. Lee, J. H. Lee, H. J. Ryu and S. H. Hong, "Enhancement of toughness and wear resistance in boron nitride nanoplatelet (BNNP) reinforced $Si_3N_4$ nanocomposites," *Scientific Reports*, vol. 6, Jun. 2016. [Online]. https://doi.org/10.1038/srep27609

[18] Y. Feng, K. Han and D. Owen, “Discrete element simulation of the dynamics of high energy planetary ball milling processes,” *Materials Science and Engineering,* Vols. 375–377, pp. 815–819, Jul. 2004. [Online]. https://doi.org/10.1016/j.msea.2003.10.162

[19] J. Li, K. Hu and Y. Zhou, “Formation of $TiB_2$/TiN nanocomposite powder by high energy ball milling and subsequent heat treatment,” *Materials Science and Engineering,* vol. A326, pp. 270–275, Mar. 2002. [Online]. https://doi.org/10.1016/S0921-5093(01)01499-X

[20] D. Witkin and E. Lavernia, “Synthesis and mechanical behavior of nanostructured materials via cryomilling,” *Progress in Materials Science,* vol. 51, pp. 1–60, Jan. 2006. [Online]. https://doi.org/10.1016/j.pmatsci.2005.04.004

[21] S. Polat, Y. Sun, E. Cevik, H. Colijn and M. E. Turan, “Investigation of wear and corrosion behavior of graphene nanoplatelet-coated $B_4C$ reinforced Al–Si matrix semi-ceramic hybrid composites,” *Journal of Composite Materials,* vol. 53, no. 25, pp. 3549–3565, Apr. 2019. [Online]. https://doi.org/10.1177/0021998319842297

[22] D. Berman, A. Erdemir and A. V. Sumant, “Graphene: a new emerging lubricant,” *Materials Today,* vol. 17, no. 1, pp. 31–42, Feb. 2014. [Online]. https://doi.org/10.1016/j.mattod.2013.12.003

[23] J. Davis, “Alloying: Understanding the Basics,” Materials Park, OH, USA: ASM International, Dec. 2001, pp. 351–416.

[24] S. Yin, P. Cavaliere, B. Aldwell, R. Jenkins, H. Liao, W. Li and R. Lupoi, “Cold spray additive manufacturing and repair: Fundamentals and applications,” *Additive Manufacturing,* vol. 21, pp. 628–650, May 2018. [Online]. https://doi.org/10.1016/j.addma.2018.04.017

[25] A. International, *Standard Practice for Operating Salt Spray (Fog) Apparatus,* West Conshohocken, PA, USA: 2011.

[26] P. Lv, M. N. Guzik, S. Sartori and J. Huot, “Effect of ball milling and cryomilling on the microstructure and first hydrogenation properties of TiFe+4 wt.% Zr alloy,” *Jour. Of Mat. Res. And Techn.,* vol. 8, no. 2, pp. 1828–1834, Apr. 2019. [Online]. https://doi.org/10.1016/j.jmrt.2018.12.013

[27] A. Nieto, J. M. Zhao, Y.-H. Han, K. H. Hwang and J. M. Schoenung, “Microscale tribological behavior and in vitro biocompatibility of graphene nanoplatelet reinforced alumina,” *Journal of the Mechanical Behavior of Biomedical Materials,* vol. 61, pp. 122–134, Aug. 2016. [Online]. https://doi.org/10.1016/j.jmbbm.2016.01.020

[28] Z. Zhang, F. Liu, E.-H. Han and L. Xu, “Mechanical and corrosion properties in 3.5% NaCl solution of cold sprayed Al-based coatings,” *Surface and Coatings Technology*, vol. 386, Mar. 2020. [Online]. https://doi.org/10.1016/j.surfcoat.2020.125372

[29] C. Xie, H. Li, X. Zhou and C. Sun, “Corrosion behavior of cold sprayed pure zinc coating on magnesium,” *Surface and Coatings Technology*, vol. 374, pp. 797–806, Sep. 2019. [Online]. https://doi.org/10.1016/j.surfcoat.2019.06.068

[30] K. Xhanari and M. Finsgar, “Organic corrosion inhibitors for aluminum and its alloys in chloride and alkaline solutions: A review,” *Arabian Journal of Chemistry*, vol. 12, pp. 4646–4663, Dec. 2019. [Online]. https://doi.org/10.1016/j.arabjc.2016.08.009

# INITIAL DISTRIBUTION LIST

1. Defense Technical Information Center
   Ft. Belvoir, Virginia

2. Dudley Knox Library
   Naval Postgraduate School
   Monterey, California